A thesis submitted in partial fulfillment
for the degree of Bachelor of Engineering

On the influence of coregistration errors on satellite image pansharpening methods

by Maximilian Langheinrich

Degree program: *Geoinformatics and satellite positioning*

Supervisors:
Prof. Dr. Peter Krzystek (University of Applied Sciences, Munich)
Dr. Tobias Storch (German Aerospace Agency)

In cooperation with:
Department Photogrammetry and Image Analysis
Remote Sensing Technology Institute, German Aerospace Center

Winter semester 2013/2014
Closing date: 05.05.2014

Acknowledgements

Very much gratitude to Prof. Dr. Peter Krzystek (University of Applied Sciences Munich) and Dr. Tobias Storch (German Aerospace Center) for supervising my thesis. I also want to thank the whole staff of the Remote Sensing Technology Institute for supporting me with scientific advice and cake and enabling me a very enjoyable time at the German Aerospace Center.

Attachments

Contents

Chapter 1

Introduction

Since the advent of remote sensing it has evolved into a broad field of research, contributing to many sciences and commercial applications. The number of active Earth observation satellites and new sensor technologies steadily grows and one of the permanently most pursued aims is surely the enhancement of ground resolution. Modern imaging satellites are able to provide images with a sub-meter ground sampling distance. GeoEye-1 as the currently best performing operational commercial satellite delivers a resolution of 0.41 m (although the data is typically downgraded to 0.5 m due to US-American export regulations). In the near future projects like WorldView 3 will be able to acquire images with an even higher resolution of 0.31 m. On the other hand the development of platforms featuring a high spectral resolution, like e.g. the upcoming EnMAP satellite (observing with 232 spectral bands), is an important necessity in regard to the improvement of remote sensing applications.

Sensors capable of obtaining data with a high geometric resolution come with the drawback of lacking detailed spectral information. Their relative reflective response functions usually cover the visible and near infrared spectrum of light, referred to as panchromatic spectrum, realized as a gray value intensity image of the Earth's surface. Sensors able to distinguish between multiple bands of wavelengths, so called multi-spectral and hyper-spectral instruments, on the contrary, have a lower spatial resolution, due to engineering implementation and physical constraints.

As remote sensing applications ideally use images featuring both, a high geometric and spectral resolution, many efforts have been made over the past three decades to develop and enhance techniques to fuse panchromatic and multi-spectral data into one high resolution multi-band image. Supported by the increasing performance of computers, knowledge in the field of computer vision and the fact that Earth observation platforms nowadays typically carry both types of above mentioned

sensors, many effective methods evolved. The technical term for fusion processes of this kind is generally known as pansharpening.

1.1 Objectives of thesis

The aim of the on hand thesis, besides giving a small overview of commonly used pansharpening methods, is to address the implicit problems of satellite image fusion, especially those generated by potentially defective input data due to technical issues and/or deficient calibration and processing of the underlying platforms instruments. In particular the influence of co-registration errors of image data on the outcome of two different pansharpening approaches will be analyzed, namely GIHS (Generalized Intensity-Hue-Saturation fusion) and SCFF (Spectrally Consistent Fusion Framework).

While suppliers of satellite images usually provide co-registered scenes, as they have access to the exact technical specifications of their platforms, this cannot be taken for granted. Further it is common practice to co-register scenes from different missions, which poses a certain challenge. A detailed overview is given of how pansharpening results can be evaluated and in which range of co-regsitration errors the outcome suffers from measureable quality losses. Further the two presented image fusion techniques are analyzed regarding their individual sensitivity concerning mismatches of satellite image pairs from different sensors.

An additional objective of this work is to detect if the pansharpened images are viable for different kinds of constitutive processing. Hence the outcome of atmospheric correction and vegetation classification via index application is evaluated.

1.2 State of the art

According to a survey of pansharpening methods from 2011 [3] satellite image fusion techniques can be categorized into five groups: component substitution, relative reflective contribution, high-frequency injection, methods based on the statistics of an image and multiresolution image fusion. As stated by the authors, "note that although the proposed classification defines five categories [...] some methods can be classified in several categories and, so, the limits of each category are not sharp and there are many relations among them"[3, p. 5]. GIHS as one of the methods used in this thesis can be assigned to the family of componen substitution techniques. SCFF on the other hand can be seen as a combination of releative reflective contribution and high-frequency injection. More recent developments aim in the direction of e.g.

finding new ways of solving the pansharpening problem, like SparseFI (Sparse Fusion of Images)[16] or try to improve common fusion techniques and their computational performance in order to apply them to hyperspectral image data [6].

1.3 Main results of thesis

The results of the analysis conducted in the frame of this work show that the two presented fusion techniques behave different in every aspect examined. SCFF produces better pansharpening results concerning maintenance of spectral information while GIHS method on the other hand excels in the preservation of spatial resolution. In general SCFF delivers the more satisfying overall result. This evaluation applies when working with properly co-registered input data. In the presence of even small co-registration errors, the performance of the two methods flips compared to each other, showing that GIHS is much more stable against (increasing) mismatches. It is also shown that the decrease of pansharpening result quality occurs periodically and scales linear with a growing co-registration error. Regarding the last aspect of higher-level processing of the fused images, it is observed that results processed by SCFF show the same behaviour to atmospheric correction and index application as the original multispectral source data. GIHS may deliver false outcomes in both fields due to the inherent color-shift caused by this method.

1.4 Structure of thesis

Beginning with chapter 2 an overview of the used optical satellite images of the Japanese ALOS mission, the specific test areas and the underlying sensors is given. Here one can get a glimpse of what problems may occur during the pansharpening process depending on particular specifications of the different sensors. Then in chapter 3 the two employed pansharpening methods are explained, showing their theory and algorithmic realization. In chapter 4 these methods are applied to the image data and general results of the processes are shown, and the computing performance of the two pansharpening algorithms is evaluated. The following discussion in chapter 5 aims to reveal the main problems occurring when inaccurately registered images are used and where they are rooted in. Additionally it is argued how potential color distortions further influence follow-up products, especially concerning atmospheric correction and indices. Finally the conclusion sums up the gained insights and gives an outlook on possible developments concerning pansharpening in chapter 6.

Chapter 2

Optical remote sensing data

The optical data used in this thesis and provided by ESA (European Space Agency) consists of four satellite imaging scenes taken by sensors aboard the ALOS (Advanced Land Observing Satellite) mission. ALOS was operated by JAXA (Japan Aerospace Exploration Agency) from 24 January 2006 to 12 May 2011, mainly for cartography and disaster monitoring purposes. Three Earth observation sensors were carried by the platform: PRISM (Panchromatic Remote-Sensing Instrument for Stereo Mapping), AVNIR-2 (Advanced Visible and Near Infrared Radiometer type 2) and PALSAR (Phased Array type L-band Synthetic Aperture Radar). All technical specifications displayed are publicly available in [5].

TABLE 2.1: PRISM specifications

Number of Bands	1 (Panchromatic)
Wavelength	0.52 to 0.77 micrometers
Number of Optics	3 (Nadir; Forward; Backward)
Base-to-Height ratio	1.0 (between Forward and Backward view)
Spatial Resolution	2.5m (at Nadir)
Swath Width	70km (Nadir only) / 35km (Triplet mode)
S/N	>70
MTF	>0.2
Number of Detectors	28000 / band (Swath Width 70km) 14000 / band (Swath Width 35km)
Pointing Angle	-1.5 to +1.5 degrees (Triplet Mode, Cross-track direction)
Quantization	8 bits

Table 2.2: AVNIR-2 specifications

Number of Bands	4
Wavelength	Band 1 : 0.42 to 0.50 micrometers Band 2 : 0.52 to 0.60 micrometers Band 3 : 0.61 to 0.69 micrometers Band 4 : 0.76 to 0.89 micrometers
Spatial Resolution	10m (at Nadir)
Swath Width	70km (at Nadir)
S/N	>200
MTF	Band 1 through 3 : >0.25 Band 4 : >0.20
Number of Detectors	7000/band
Pointing Angle	- 44 to + 44 degrees
Quantization	8 bits

For the analysis in this work only data from PRISM and AVNIR-2 were used. There is a related image fusion process to pansharpening called radar-sharpening which utilizes SAR data to enhace images from optical sensors e.g. to recreate spatial information in a panchromatic image with high cloud density [8, p. 315]. This topic is however not part of the on hand thesis and only mentioned for the sake of completeness.

One reason why scenes obtained by the ALOS platform were chosen as source data were the characteristic response functions of the optical sensors (Figure 2.1). The low correlation between the blue band and the panchromatic band as well as the near-infrared band and the panchromatic band offer an ideal basis for the analysis of the pansharpening behavior of different methods. Many state-of-the-art optical satellite imaging sensors have different characteristics concerning their relative spectral response. Further the different quality of estimation of high-resolution DNs in the blue band especially affects the results of particular higher-level processing applications such as atmospheric correction.

A second reason is the fact that the scenes of the different sensors are not well co-registered to each other by the provider (unlike data obtained by Earth observation satellites like WorldView 2). This involves that the individual user may have to co-register the panchromatic and multispectral scenes by himself which can be a source of significant systematic errors. Even modern processing chains for satellite

image data can be inaccurate to a certain degree. That arises the need for the analysis in this thesis to detect a link between flawed co-registration and pansharpening outcomes. In the case of the data on hand the processing is performed by ESA using a processing chain developed by the DLR (German Aerospace Agency). The original data as received from JAXA featuring the product level 1B1 first of is processed regarding radiometric corrections resulting in a higher product level dataset of type 1C. Then orthorectification is applied to correctly match, geocode and project the optical satellite imaging scenes. This is done by considering attitude and position of the satellite, the PRISM and AVNIR-2 sensor models and mounting angles (Boresight Alignment), the DEM (Digital Elevation Model) intersection model, map projection model and resampling model. In the last step further enhancements like sensor model parameter improvement and RPC (Rational Polynomial Functions) generation are applied.

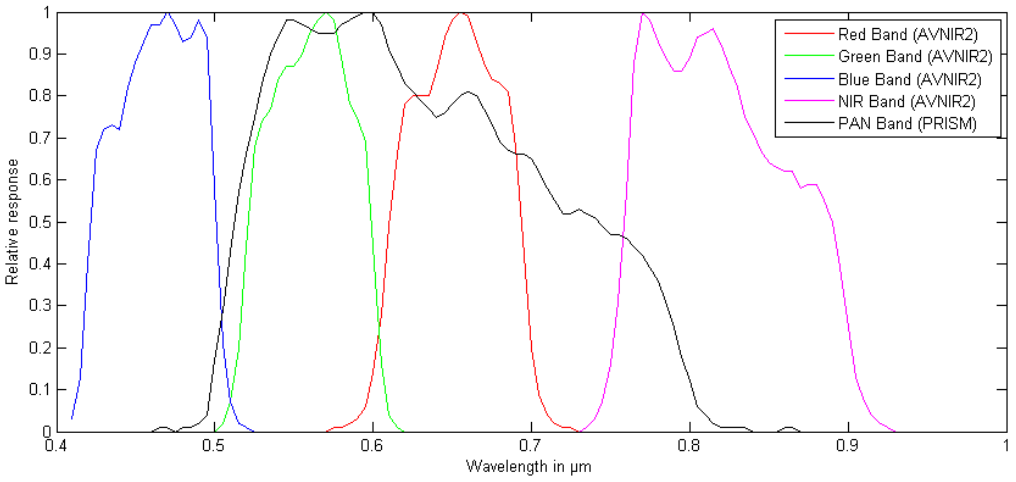

FIGURE 2.1: Relative response functions of AVNIR-2 and PRISM (nadir only mode) sensors

The decision on the two particular on hand scenes was made by means of diversity concerning ground features. From each image six characteristic test areas were picked, trying to achieve a high level of distinction in building density, plant cover and natural water content between the single areas. The panchromatic images in both scenes were photographed by the PRISM sensor in nadir only mode. The multispectral scenes were obtained by the AVNIR-2 sensor.

Depicting the "Five Lake Region" in upper Bavaria, Germany, the first scene (Figure 2.2) features large spaces of central European vegetation and agriculture

like deciduous, coniferous and mixed forest, wheat, corn, rapeseed, et cetera. It was obtained on the 14th June 2007 (AVNIR-2: 10:20:41.28 UTC / PRISM: 10:19:56.13 UTC). On the right border, parts of Munich were observed, mostly western and southwestern suburbia, which offer good examples for urban environment. The test area containing water coverage includes a part of the Woerth lake.

In contrast to the continental climate region of Germany, the second scene shows the coastal city of Tunis, Tunesia on the 14th November 2010 (AVNIR-2: 10:11:36.05 UTC / PRISM: 10:11:36.06 UTC), surrounded sparsely populated hilly landscape and bordering on the Mediterranean in the northeast. Test areas differ between typical urban structures, inner harbour, and and in the farther southwest of the city a mountain range and arid agriculture. Therefore the individual sample regions of the images not only vary within the scenes but also in an inter-image sense, which again is a good foundation for the upcoming analysis.

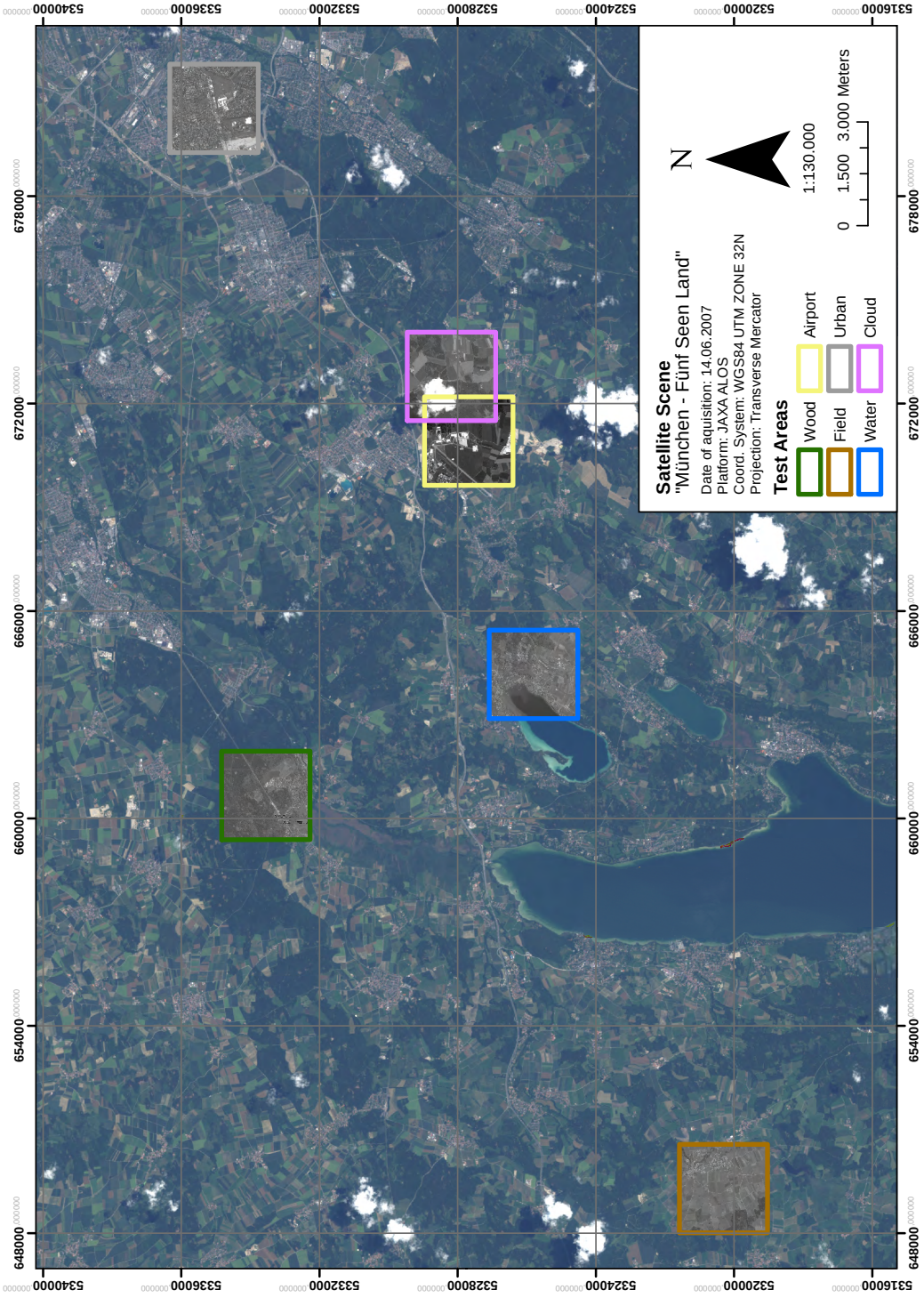

FIGURE 2.2: Part of ALOS satellite scene over Munich with test areas

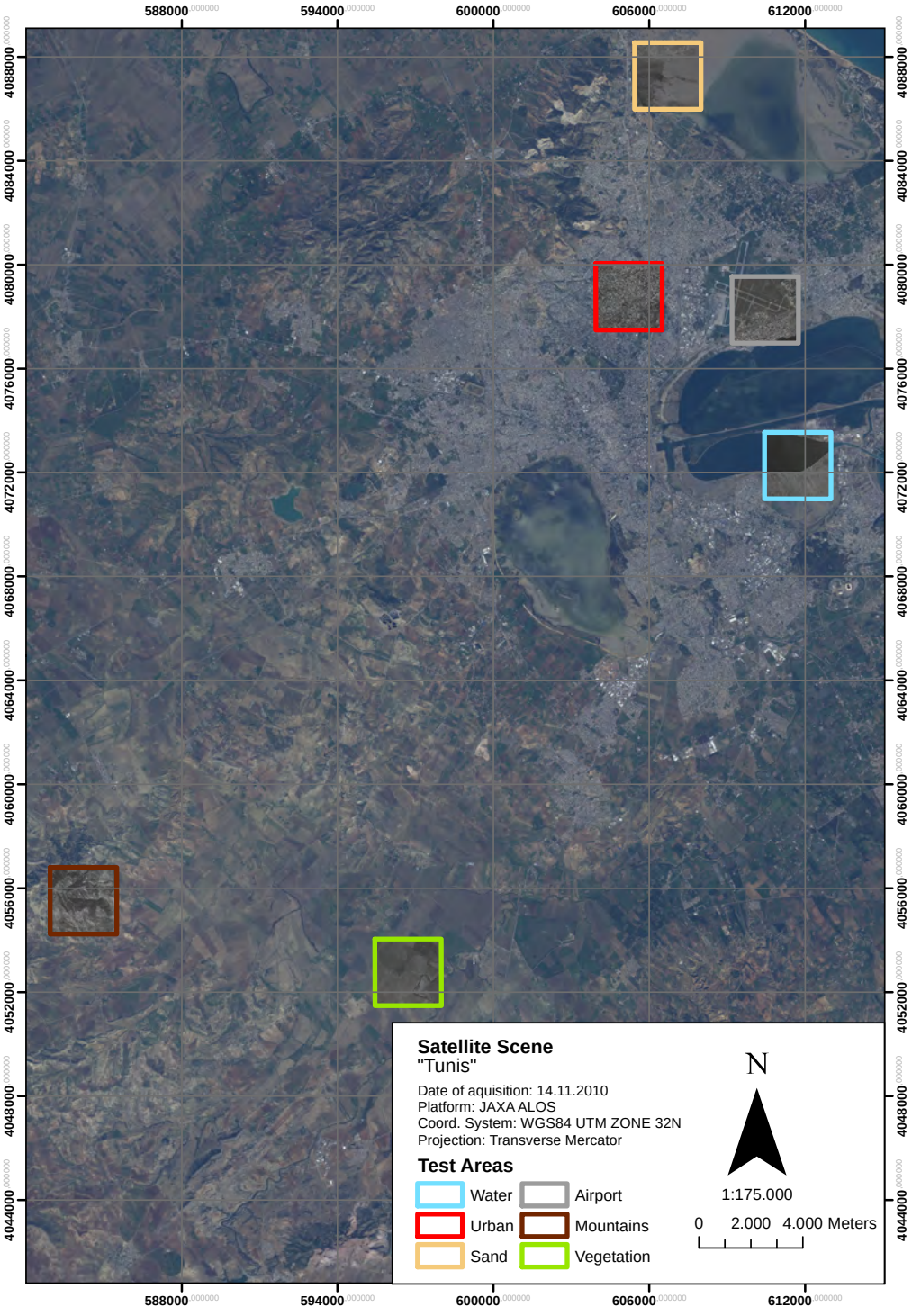

FIGURE 2.3: Part of ALOS satellite scene over Tunis with test areas

Chapter 3

Pansharpening methods

In the course of this work two specific pansharpening methods were employed to produce high-resolution images. The GIHS is an advanced variant of the basic Intensity-Hue-Saturation image fusion method. The SCFF is a rather novel approach to pansharpening with its attention turned on maintaining complete and correct spectral information in the resulting data. These methods were intentionally chosen for their elementary differences in how they solve the image fusion problem. In the following sections the characteristics of each will be described in detail.

3.1 GIHS

The first approach used in this thesis is the IHS technique which has been used in the remote sensing context since 1987 [3] and is one of the most common methods in commercial software solutions. It queues in the category of component substituton procedures and stands out due to its fairly straightforward functionality. The pixelwise process can be expressed by the following equations, as described in [10].

1. The multi-spectral image is upsampled to the resolution of the panchromatic image. In the course of this thesis, upsampling at this step is done using nearest-neighbour interpolation to avoid a pre-pansharpening spectral distortion effect.

2. Then a transformation in the IHS colorspace is conducted.

$$\begin{bmatrix} I \\ v1 \\ v2 \end{bmatrix} = \begin{bmatrix} \frac{1}{3} & \frac{1}{3} & \frac{1}{3} \\ -\frac{\sqrt{2}}{6} & -\frac{\sqrt{2}}{6} & \frac{2\sqrt{2}}{6} \\ \frac{1}{\sqrt{2}} & -\frac{1}{\sqrt{2}} & 0 \end{bmatrix} \begin{bmatrix} R \\ G \\ B \end{bmatrix} \tag{3.1}$$

where I represents the intensity part of the pixel and $v1$, $v2$ the corresponding hue and saturation values.

3. The intensity part of the IHS image is substituted by the PAN image. The reverse transformation results in a high-resolution RGB image.

$$\begin{bmatrix} R_{HR} \\ G_{HR} \\ B_{HR} \end{bmatrix} = \begin{bmatrix} 1 & -\frac{1}{\sqrt{2}} & \frac{1}{\sqrt{2}} \\ 1 & -\frac{1}{\sqrt{2}} & -\frac{1}{\sqrt{2}} \\ 1 & \sqrt{2} & 0 \end{bmatrix} \begin{bmatrix} PAN \\ v1 \\ v2 \end{bmatrix} \tag{3.2}$$

As the whole calculation can be rewritten into a single, pixelwise addition (3.3), one advantage of this method lies in its high computational efficiency. Further the spatial information of the PAN image is completely induced into the multi-band image, which results in a high geometric accuracy.

On the other hand IHS image fusion is very susceptible to a main problem of pansharpening. In order to generate spectrally consistent high-resolution RGB data, an appropriate correlation between the relative response functions of the single bands of the multi-spectral sensor and the panchromatic band is necessary. In practice such a congruency is seldom achieved. This results in a color shift of the pansharpened image and accordingly in a falsification of the pristine spectral information. Depending on the degree of band correlation the color shift is stronger or less intense and thus more or less optically recognizable. Another inherent issue is that the transformation as it is displayed in equation (3.1) and (3.2) can only be applied to three channels, by default the RGB combination of a multi-band sensor.

As mentioned earlier, the IHS transformation can be expressed as described in [10], [11]:

$$\begin{aligned} \begin{bmatrix} R_{HR} \\ G_{HR} \\ B_{HR} \end{bmatrix} &= \begin{bmatrix} 1 & -\frac{1}{\sqrt{2}} & \frac{1}{\sqrt{2}} \\ 1 & -\frac{1}{\sqrt{2}} & -\frac{1}{\sqrt{2}} \\ 1 & \sqrt{2} & 0 \end{bmatrix} \begin{bmatrix} I + (PAN - I) \\ v1 \\ v2 \end{bmatrix} \\ &= \begin{bmatrix} 1 & -\frac{1}{\sqrt{2}} & \frac{1}{\sqrt{2}} \\ 1 & -\frac{1}{\sqrt{2}} & -\frac{1}{\sqrt{2}} \\ 1 & \sqrt{2} & 0 \end{bmatrix} \begin{bmatrix} I + \delta \\ v1 \\ v2 \end{bmatrix} = \begin{bmatrix} R + \delta \\ G + \delta \\ B + \delta \end{bmatrix} \end{aligned} \tag{3.3}$$

where

$$\delta = PAN - I. \tag{3.4}$$

This conversion not only enhances the computation speed of the whole procedure, but also enables to get rid of the afore described three channel constraint. The last

transformation term as proposed in [10] is extended to the form:

$$\begin{bmatrix} R_{HR} \\ G_{HR} \\ B_{HR} \\ NIR_{HR} \end{bmatrix} = \begin{bmatrix} R + \delta_4 \\ G + \delta_4 \\ B + \delta_4 \\ NIR + \delta_4 \end{bmatrix} \tag{3.5}$$

where

$$\delta_4 = PAN - (R + G + B + NIR)/4. \tag{3.6}$$

with

R, G, B, NIRdenoting the red, green, blue and near infrared band of the AVNIR-2 sensor.

The per-pixel intensity values of the panchromatic image are equally distributed into the individual multispectral bands. In equation 3.5 the full multispectral bandwidth of the ALOS satellite optical image data is used for the pansharpening process. This results in a smaller color shift especially in regions of dense vegetation, which feature a high spectral response in the near infrared range of wavelengths.

The GIHS pansharpening method was implemented in Matlab as follows:

```
intensityMatrix = sum((MS / bands), 3);

IMD = cat(3, PAN - intensityMatrix, ...
             PAN - intensityMatrix, ...
             PAN - intensityMatrix, ...
             PAN - intensityMatrix);

IHS = MS + IMD;
```

3.2 SCFF

The second approach used in this thesis is the SCFF (Spectrally Consistent Fusion Framework) as proposed by H. Aanæs et al. [1]. It represends a rather unique and novel method which "is model based, and the fused images obtained spectrally are consistent by design"[1, p. 1336].

Spectral consistency is achieved by deriving a ratio vector from the sensors' response function, which describes fracture values of the single multispectral bands

contained in the panchromatic pixels:

$$\vec{R} = \begin{bmatrix} \alpha_{(1,PAN)} \\ \alpha_{(2,PAN)} \\ \vdots \\ \alpha_{(n,PAN)} \end{bmatrix} \tag{3.7}$$

where

$$\alpha_{(i,PAN)} = \frac{\langle F^i, F^{PAN} \rangle}{\sqrt{\langle F^i, F^i \rangle \langle F^{PAN}, F^{PAN} \rangle}} \tag{3.8}$$

with

$$i \in \{1 \dots n(\text{Total number of multispectral bands})\}$$

The inner product $\langle F^i, F^{PAN} \rangle$ represents the integral over the spectral response functions of a certain range of wavelengths Ω of the corresponding multispectral band and the panchromatic sensor:

$$\langle F^i, F^{PAN} \rangle = \int_{\Omega} F^i(\omega) F^{PAN}(\omega) d\omega \tag{3.9}$$

This, as seen in the equations above, opens up the possibility to address every band of the multispectral sensor to generate a fused image. For the proper calculation of the ratio vector a previous knowledge of the exact relative spectral response functions of the applied sensor must be postulated. In the course of the on hand thesis $\vec{R}$ for the ALOS AVNIR-2 sensor with respect to the panchromatic channel of ALOS PRISM (nadir only mode) was calculated as:

$$\vec{R}_{AVNIR2} = \begin{bmatrix} \alpha_{Blue} \\ \alpha_{Green} \\ \alpha_{Red} \\ \alpha_{NIR} \end{bmatrix} = \begin{bmatrix} 0.015 \\ 0.688 \\ 0.606 \\ 0.174 \end{bmatrix}$$

In the next step for each pixel i in the multispectral image, sixteen corresponding multispectral pixels $i, j, j \in [1, \dots, 16]$ containing the spatial information of the panchromatic image are generated by weighing the panchromatic intensity data with the before determined ratio vector. The number of exactly sixteen corresponding pixels for each multispectral pixel i is derived from the $1:16$ ratio of the 10m $\times$ 10 m ground resolution of the AVNIR-2 sensor and the 2.5 m $\times$ 2.5 m ground resolution

of PRISM.

$$\begin{bmatrix} \Delta I_{ij}^{Blue} \\ \Delta I_{ij}^{Green} \\ \Delta I_{ij}^{Red} \\ \Delta I_{ij}^{NIR} \end{bmatrix} = \begin{bmatrix} \alpha_{Blue} \\ \alpha_{Green} \\ \alpha_{Red} \\ \alpha_{NIR} \end{bmatrix} (P_{ij}^{HR} - P_i^{\mu}) \tag{3.10}$$

with

$$P_i^{\mu} = \frac{\sum_{j=1}^{16} P_{ij}^{HR}}{16}.$$

One important aspect of equation 3.10 is the subtraction of P_i^{μ}, which denotes the mean of the sixteen pixels corresponding to the low resolution pixel i. It results in a relative description of the spatial frequency of the relevant high-resolution four-by-four pixel region.

Image fusion is then conducted by infusing the spatial information pixel by pixel into the multispectral image through addition:

$$\begin{bmatrix} B_{ij}^{HR} \\ G_{ij}^{HR} \\ R_{ij}^{HR} \\ NIR_{ij}^{HR} \end{bmatrix} = \begin{bmatrix} B_i^{LR} \\ G_i^{LR} \\ R_i^{LR} \\ NIR_i^{LR} \end{bmatrix} + \begin{bmatrix} \Delta I_{ij}^{Blue} \\ \Delta I_{ij}^{Green} \\ \Delta I_{ij}^{Red} \\ \Delta I_{ij}^{NIR} \end{bmatrix} \tag{3.11}$$

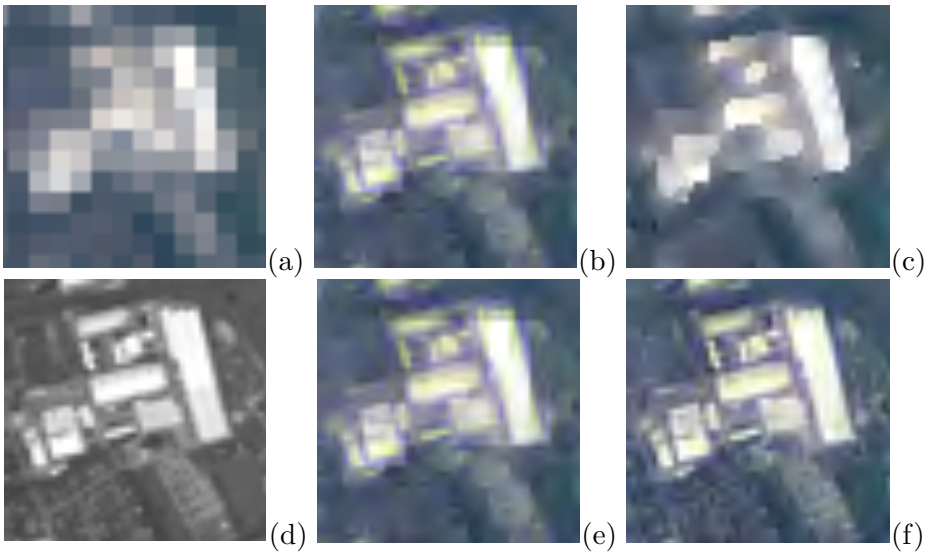

FIGURE 3.1: (a) Original multispectral image (d) Original panchromatic image (b) Fusion result by equation 3.11 (c) Result using canny edge based smoothing algorithm (e) Result using gradient based smoothing algorithm (f) Result using smoothing algorithm developed in this thesis

As proofed in [1] the resulting high-resolution images offer spectral consistency but also suffer from a rather blocky appearence (compare Figure 3.1b). To further enhance the visual appearance while sustaining spectral resolution, the authors of [1] introduce different smoothing algorithms by weighing singular pixels by edge and gradient extraction of the spatial data (Figure 3.1c & d).

The results of this further processing where decided to be insufficient for the thesis at hand, as they tend to blur the final image data while weirdly emphasizing structural edges.

Therefore a new algorithm to reduce the induced block artifacts was developed, aiming to maintain spectral consistent band intensities and achieving best possible spatial resolution alike. To accomplish this, high resolution result images from both presented fusion methods were used. The spectrally consistant (though blocky) pansharpened image and the GIHS image are processed by a sliding-window operation using a three-by-three window. In both cases the mean of each respective window is calculated and the GIHS mean value is substracted from the SCFF mean value. The difference is then added to the GIHS pixel corresponding to the center pixel of the actual window position. Thereby an enhancement is applied to every pixel of the GIHS image, derived from the SCFF image. This process induces a very high spatial accuracy compared to the above mentioned smoothing techniques, while improving the intensity of each band of the GIHS image to near spectrally consistent quality (as shown in Figure 3.1f). The pixelwise approach, which needs to be employed for each band separately, can be mathematically represented as:

$$P_{ij}^{HR'} = P_{ij}^{GIHS} + \mu_{ij} \tag{3.12}$$

with

$$\mu_{ij} = \frac{\sum\limits_{k \in W_{ij}} P_k^{SCFF}}{9} - \frac{\sum\limits_{k \in W_{ij}} P_k^{GIHS}}{9} \tag{3.13}$$

W_{ij} denotes the eight-neighbourhood with respect to the high-resolution image over the centerpixel P_{ij}. The application of a sliding window entails that the border-pixels of the used images can not be considered in this step. The prior SCFF images as well as the representative images of the proposed canny and gradient based weighting algorithms [1] were generated in Matlab using the code provided on the main authors website [2]. The improved smoothing algorithm was developed in MatLab as well:

```
wait = waitbar(0, 'Smoothing Image ...');

blockCalc = @(x, y) mean(mean(x)) - mean(mean(y));
```

```
for row = 1:size(RGBconsistent, 1)
    for col = 1:size(RGBconsistent, 2)
        if row == 1 && col == 1
            PANSHARP(row, col, :) = IHS(row, col, :) + ...
            blockCalc(RGBconsistent(row:row+1, col:col+1, :), ...
            IHS(row:row+1, col:col+1, :));
        elseif row == 1 && col == size(RGBconsistent, 2)
            PANSHARP(row, col, :) = IHS(row, col, :) + ...
            blockCalc(RGBconsistent(row:row+1, col-1:col, :), ...
            IHS(row:row+1, col-1:col, :));
        elseif row == size(RGBconsistent, 1) && col == 1
            PANSHARP(row, col, :) = IHS(row, col, :) + ...
            blockCalc(RGBconsistent(row-1:row, col:col+1, :), ...
            IHS(row-1:row, col:col+1, :));
        elseif row == size(RGBconsistent, 1) && col == size(RGBconsistent, 2)
            PANSHARP(row, col, :) = IHS(row, col, :) + ...
            blockCalc(RGBconsistent(row-1:row, col-1:col, :), ...
            IHS(row-1:row, col-1:col, :));
        elseif row == 1
            PANSHARP(row, col, :) = IHS(row, col, :) + ...
            blockCalc(RGBconsistent(row:row+1, col-1:col+1, :), ...
            IHS(row:row+1, col-1:col+1, :));
        elseif col == 1
            PANSHARP(row, col, :) = IHS(row, col, :) + ...
            blockCalc(RGBconsistent(row-1:row+1, col:col+1, :), ...
            IHS(row-1:row+1, col:col+1, :));
        elseif col == size(RGBconsistent, 2)
            PANSHARP(row, col, :) = IHS(row, col, :) + ...
            blockCalc(RGBconsistent(row-1:row+1, col-1:col, :), ...
            IHS(row-1:row+1, col-1:col, :));
        elseif row == size(RGBconsistent, 1)
            PANSHARP(row, col, :) = IHS(row, col, :) + ...
            blockCalc(RGBconsistent(row-1:row, col-1:col+1, :), ...
            IHS(row-1:row, col-1:col+1, :));
        else
            PANSHARP(row, col, :) = IHS(row, col, :) + ...
            blockCalc(RGBconsistent(row-1:row+1, col-1:col+1, :),...
            IHS(row-1:row+1, col-1:col+1, :));
        end
    end
    waitbar(row/size(RGBconsistent, 1), wait);
end
```

Chapter 4

Experiments

4.1 Quality metrics

In the of the evaluation of pansharpened images two different factors of quality must be considered. On one hand it must be measured how much of the geometric information contained in the high-resolution panchromatic image was successfully induced into the fused image, on the other hand the degree of accuracy concerning the reconstruction of the original spectral characteristics of a optical remote sensing scene has to be described. In both cases a first, reliable judgement can be made by human vision to identify gross errors. But with deviations growing smaller, especially in the case of color shifts, the human eye fails to recognize differences.

Therefore many efforts has be made to develop dependable quality metrics to detect even small changes in the image structure. For the analysis at hand four commonly used indicators were used to review the results of the introduced pansharpening methods. For the evaluation of spatial similarity the correlation coefficient[4, p. 1596] is used, which resembles a widely applied statistical metric concerning interrelation between two different parameters. Addressing the quantitation of spectral consistency quality is expressed by SAM (Spectral Angle Mapper)[4, p. 1597], which is used in many different remote sensing applications. Approaching the more special case of pansharpening in particular, two further indices were chosen, aiming to provide a simple, combined quality metrics concerning image fusion results. By name these are ERGAS (Erreur Relative Globale Adimensionelle de Synthèse) as proposed in [13] and Q-Index introcuded in [14].

In order to detect geometric similarity, high-frequency spatial information has to be extracted from the images to be compared. Therefore every single band of the pansharpened image (PS) and the reference image (R) are convoluted with a

high-pass filter shown in equation 4.1. Border-pixels are treated by means of border replication.

$$HPF = \begin{bmatrix} -1 & -1 & -1 \\ -1 & 8 & -1 \\ -1 & -1 & -1 \end{bmatrix} \tag{4.1}$$

Then the correlation coefficient for each pair of corresponding band of fused and high-resolution reference image is calculated.

$$\mathrm{CC} = \frac{\sigma_{R,PS}}{\sigma_R * \sigma_{PS}} \tag{4.2}$$

with

σ_R = unbiased standard deviation of reference image (HR PAN)

σ_{PS} = unbiased standard deviation of pansharpened image

$\sigma_{R,PS}$ = unbiased covariance between reference and pansharpened image

By determining the mean of the CCs of the single bands an overall validation is given ranging from -1 (negative correlation) to 1 (positive correlation) as the best possible outcome.

SAM denotes the angular difference between two spectra. The spectral characteristics of a pixel are given by the individual combination of DNs (digital numbers) considering all bands. This combination can be expressed as a vector. By generating spectral vectors of a corresponding pixel pair in the reference and the fused image, its similarity can be expressed as the arccosine of the dot product between the two vectors [4][15]:

$$SAM(R, PS) = \arccos\left(\frac{\langle R, PS\rangle}{\| \vec{R} \| \cdot \| \vec{PS} \|}\right) \tag{4.3}$$

which can be written as [15]

$$SAM(R, PS) = \arccos\left(\frac{\sum_{i=1}^{n} R_i PS_i}{\sqrt{\sum_{i=1}^{n} R_i^2}\sqrt{\sum_{i=1}^{n} PS_i^2}}\right) \tag{4.4}$$

where

$$n = \text{total number of bands.}$$

Again the indicator is applied to every corresponding pixel pair and the mean for the whole scene is calculated to give an overall measure for spectral similarity. In this work SAM is given in degrees with lower angels describing better results.

With ERGAS Wald proposed a statistical overall value for judging image fusion quality, which is derived of the commonly used RMSE (Root Mean Square Error) but provides a higher robustness with respect to calibration and changes of units [13]. First the RMSE between the reference image and the pansharpened image has to be determined [4]:

$$RMSE = \sqrt{\frac{\sum_{i=1}^{M}\sum_{j=1}^{N}(R_{i,j} - PS_{i,j})^2}{M \times N}} \tag{4.5}$$

where

$$M \times N = \text{size of the images.}$$

$$R_{i,j} = \text{Pixel in row i, column j in reference image.}$$

$$PS_{i,j} = \text{Pixel in row i, column j in fused image.}$$

This is conducted bandwise, giving n RMSE values for n spectral channels. Subsequently ERGAS is obtained by the following equation [13]:

$$ERGAS = 100\frac{h}{l}\sqrt{\frac{1}{n}\sum_{i=1}^{n}\frac{RMSE_i^2}{\mu_i^2}} \tag{4.6}$$

where

$$h = \text{ground pixel resolution of HR image}$$

$$l = \text{ground pixel resolution of LR image}$$

$$\mu_i = \text{mean of intensity values in band i}$$

$$n = \text{total number of bands.}$$

Wald stated in [13, p. 102] that based on experimental observations a threshold of 3 is a representative assessment value, with results featuring lower values being of good overall quality.

As a last quality metric the Q-index introduced by Wang and Bovik was chosen. "Instead of using traditinoal error summation methods, the proposed index is designed by modeling any image distortion as a combination of three factors: loss

of correlation, luminance distortion and contrast distortion"[14, p. 81]. Therefore it gives an opportunity to review the image fusion results of the on hand thesis with a different approach. The Q-index is formulated as (again applied seperately to every single band of the sensor data):

$$Q = \frac{4 \cdot \sigma_{R,PS} \cdot \mu_R \cdot \mu_{PS}}{(\sigma_R^2 + \sigma_{PS}^2)[(\mu_R)^2 + (\mu_{PS})^2]} \tag{4.7}$$

with

$$\mu_R = \text{pixel mean value of reference image}$$

$$\mu_{PS} = \text{pixel mean value of pansharpened image}$$

Further equation 4.7 can be rearranged [14, p. 81] to depict the three factors influencing the Q-index:

$$Q = \frac{\sigma_{R,PS}}{\sigma_R \sigma_{PS}} \cdot \frac{2\mu_R \mu_{PS}}{(\mu_R)^2 + (\mu_{PS})^2} \cdot \frac{2\sigma_R \sigma_{PS}}{\sigma_R^2 + \sigma_{PS}^2} \tag{4.8}$$

Here the first component is the correlation coefficient between the reference and the fused band. The second part describes the difference of the mean luminance between R and PS and the third component measures the similiarity of contrast. As mentioned earlier the calculation of the Q-index is conducted for every corresponding band. A mean Q-index is then generated to give an overall value for general fusion quality. It can adopt values in the dynamic range of [0, 1] with one being the best value, only achieved if the two compared images are identical (this also applies for all other quality metrics).

4.2 Quality assessment

As mentioned before four optical satellite imaging scenes were chosen as the basis of the analysis. From each six test areas were picked to cover a large variety of ground features. The areas are quadratic, with a size of 1024 by 1024 pixels for the panchromatic images and 256 by 256 pixels for the lower resoluton multispectral images. In both cases this equals a ground edge length of of 2560 meters.

Regarding the evaluation conducted in this thesis one important point is mentioned. One inherent problem of the assessment of pansharpening methods is the lack of a multispectral high-resolution reference images obtained by the same sensor (as on one part this is technically not possible, on the other it would make the whole pansharpening process unnecessary)[12, p. 696]. Therefore the pansharpened

images were down-sampled by cubic interpolation to the resolution of the original multispectral image. Then the pixel values of the lower resolution multispectral image can be seen as mixed pixel values of a theoretical high-resolution multispectral image with the same spectral characteristics. A completely spectrally consistent fused image would thus, regarding the resolution ratio of the scenes used in this thesis, satisfy the criterion[1, p. 1338]:

$$\begin{bmatrix} B_i^{MS} \\ G_i^{MS} \\ R_i^{MS} \\ NIR_i^{MS} \end{bmatrix} = \frac{1}{16} \sum_{j=1}^{16} \begin{bmatrix} B_{ij}^{PS} \\ G_{ij}^{PS} \\ R_{ij}^{PS} \\ NIR_{ij}^{PS} \end{bmatrix} \tag{4.9}$$

Concerning the analysis of the results of spatial properties, the pansharpened images were compared with the original high-resolution panchromatic scene, as the geometric data available in the resulting images dervies from that source. Tables 4.1 and 4.2 show the complete list of the results.

The results in tables 4.1 and 4.2 show that the overall performance of the two chosen methods is constantly is very high regarding spectral and geometric consistency. Especially the SCFF features very good quality. Looking at the quality metrics GIHS only excels concerning the spatial correlation coefficient, which is due to the fundamental principles of operation of the two pansharpening techniques. On the other hand, concerning geometric quality SCFF only suffers from a slightly greater loss of spatial information. The four examples shown in this chapter depict the test areas in which the difference in results of the two pansharpening methods are greatest and therefore most comprehensible by human vision.

Looking at the two test areas from the "Munich" scene, it is evident that the spectral consistency achieved by GIHS is very dependent on the reflectance value and spectral combination of the multispectral channels. Although the two regions feature a high density of vegetation (Figure 4.1), which usually have a high reflectance in the near-infrared band, and big patches of water (Figure 4.2) a colour shift is merely visible by the human eye considering true color representation (which also applies to the other "Munich" test areas). This shows that for the evaluation of pansharpening results quality measures are needed to qualify and quantify the decisions which method delivers the best outcomes which may depend on the specific application. Further the two examples illustrate that it is not advisable to trivialize the performance of one particular image fusion method but to link it to the properties of the source data.

TABLE 4.1: Test areas "Munich"

	Method	CC	SAM	ERGAS	Q-index
Airport	GIHS	0.9900	1.0612	5.5045	0.9242
	SCFF	0.9222	0.4244	1.0782	0.9965
Cloud	GIHS	0.9847	1.0608	4.0250	0.9731
	SCFF	0.9169	0.4441	0.7955	0.9989
Agricult.	GIHS	0.9871	0.7983	3.1968	0.8664
	SCFF	0.9307	0.4450	1.1966	0.9714
Urban	GIHS	0.9934	1.4257	5.9481	0.8280
	SCFF	0.9186	0.8664	1.9275	0.9752
Water	GIHS	0.9860	1.2988	4.7111	0.8314
	SCFF	0.9128	0.6192	1.5558	0.9742
Forest	GIHS	0.9898	1.4249	4.9071	0.8087
	SCFF	0.9187	0.8144	1.8000	0.9666

On the contrary to the former, the two example regions from the "Tunis" scene depict that the colour shift can indeed adopt very high values. In both images, showing the Tunis airport (Figure 4.3) and a part of the northwestern city (Figure 4.4), it is clearly visible how the spectral information can change by GIHS processing. Then again SCFF performs very well concerning spectral consistancy. As said before it also achieves a relatively good amount of spatial resolution, which is also seen in the two Tunis examples as they hold a high amount of geometric structures.

It can be argued that the result images fused by SCFF appear kind of blured compared to their GIHS counterparts. As depicted in Figure 4.5, when zoomed into detail (here a magnification of 400% was applied) it arises the fact that almost the same amount of spatial information from the pansharpened image is induced into the SCFF as in the GIHS image. The impression that a blurry character of the

TABLE 4.2: Test areas "Tunis"

	Method	CC	SAM	ERGAS	Q-index
Airport	GIHS	0.9897	3.6116	7.4037	0.8210
	SCFF	0.8989	0.7966	2.1817	0.9773
Mount.	GIHS	0.9935	2.0780	4.8731	0.8562
	SCFF	0.9343	0.7393	1.6566	0.9765
Desert	GIHS	0.9911	0.8590	2.5583	0.8980
	SCFF	0.9514	0.3138	0.7785	0.9878
Urban	GIHS	0.9964	3.0470	9.7511	0.5907
	SCFF	0.9030	1.5357	3.3823	0.9184
Vege.	GIHS	0.9903	1.1007	2.8034	0.8863
	SCFF	0.9609	0.2581	0.6274	0.9875
Water	GIHS	0.9908	1.1289	3.7472	0.9433
	SCFF	0.9317	0.3495	1.1217	0.9948

SCFF image is caused by the fact that through the GIHS method a great amount of the panchromatic high-frequency data is induced into the outcome image. This leads to a high (but not compulsory to the correct) contrast with the effect of a prim appearance. The gradients in the spectrally consistent image are lower.

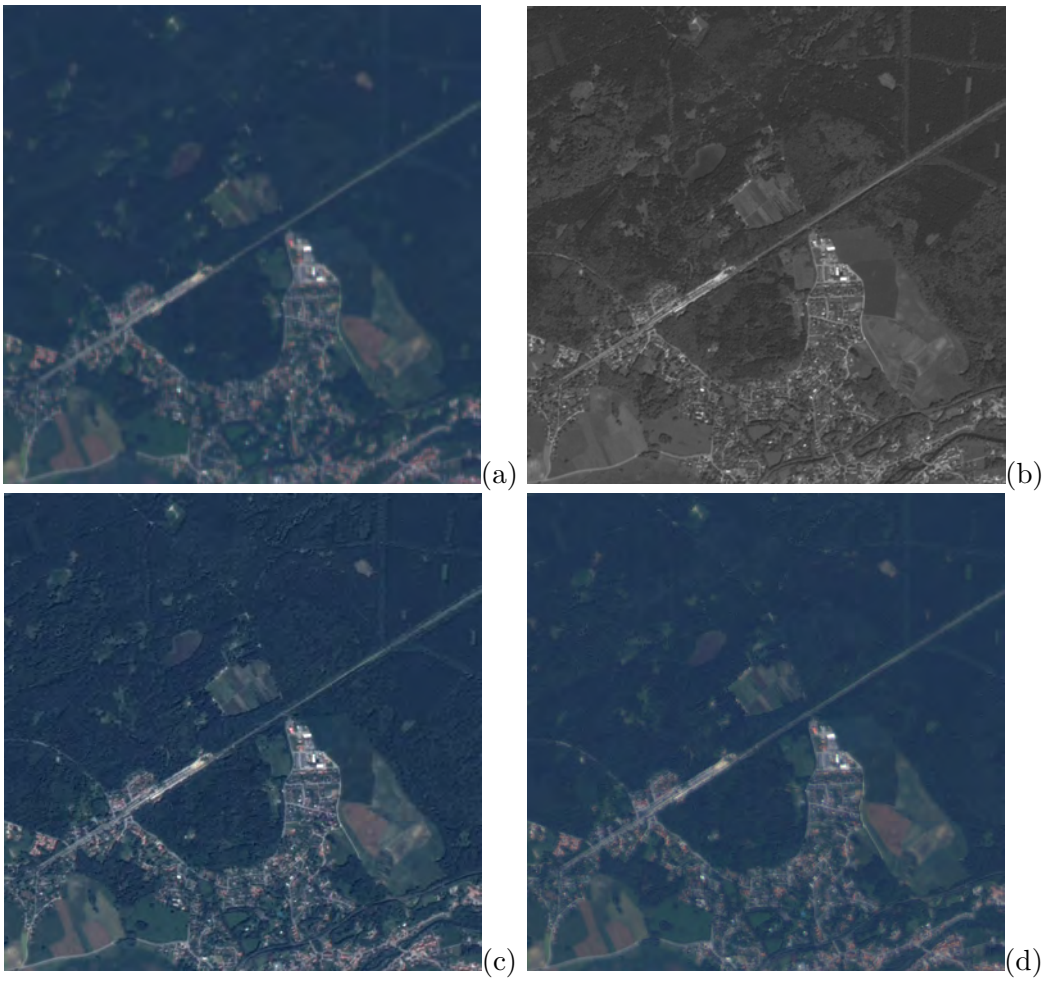

FIGURE 4.1: Test area "Munich forest": (a) AVNIR-2 multispectral image (b) PRISM panchromatic image (c) Pansharpened image using GIHS method (d) Pansharpened image using SCFF method

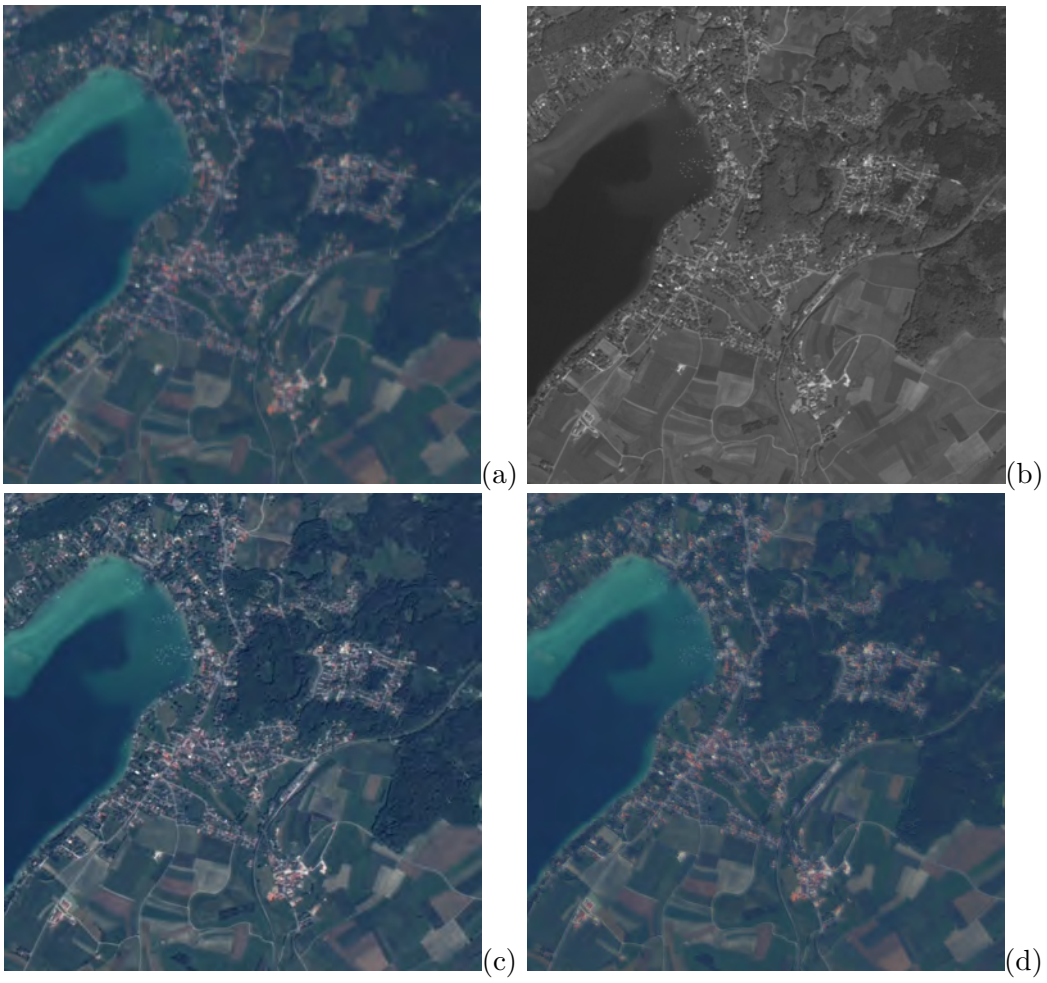

FIGURE 4.2: Test area "Munich Water": (a) AVNIR-2 multispectral image (b) PRISM panchromatic image (c) Pansharpened image using GIHS method (d) Pansharpened image using SCFF method

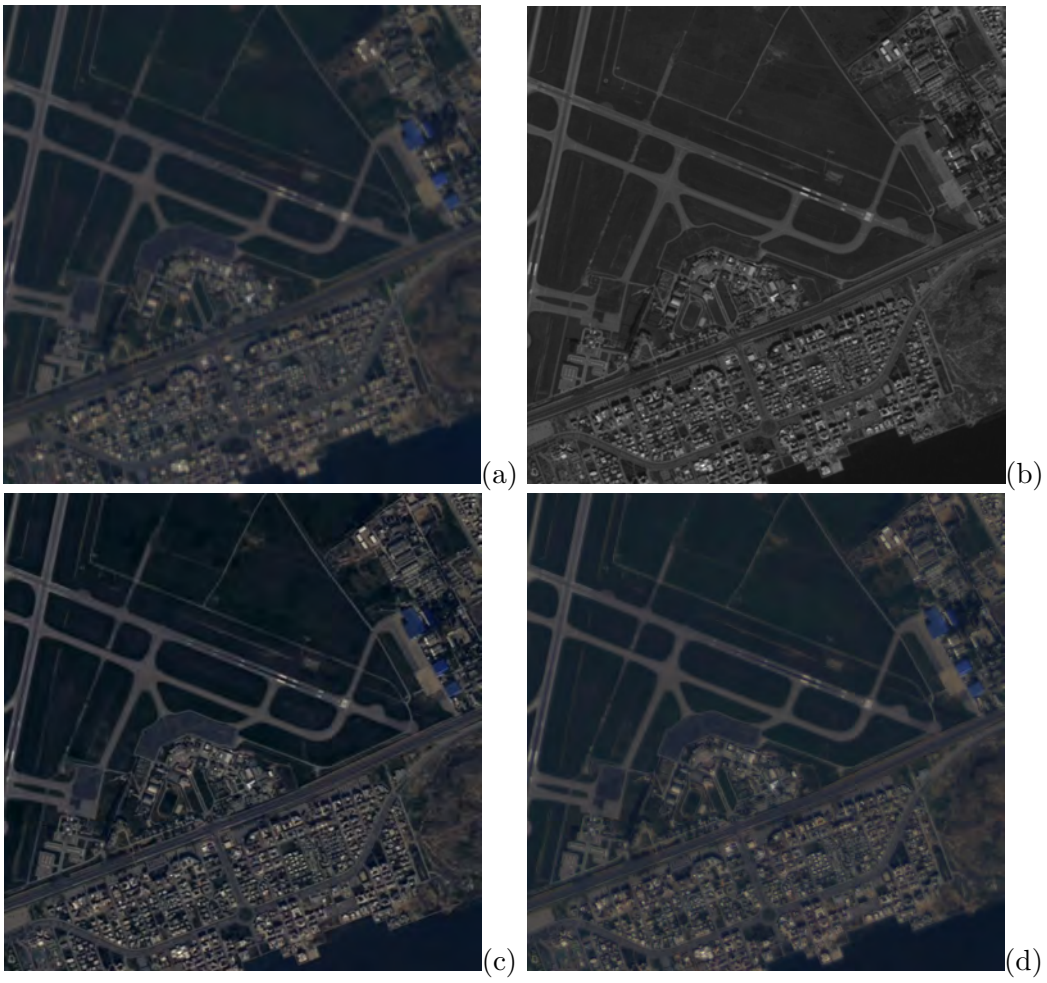

FIGURE 4.3: Test area "Tunis Airport": (a) AVNIR-2 multispectral image (b) PRISM panchromatic image (c) Pansharpened image using GIHS method (d) Pansharpened image using SCFF method

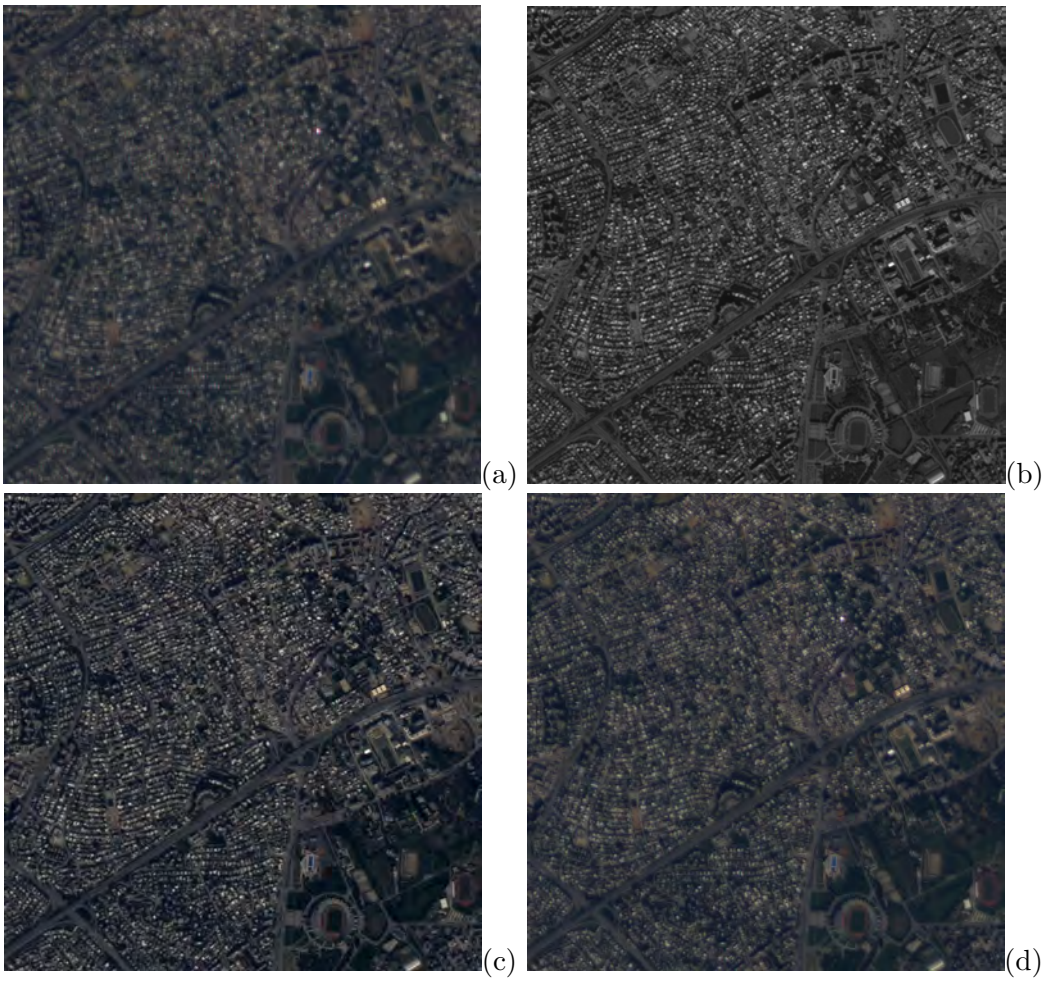

FIGURE 4.4: Test area "Tunis Urban": (a) AVNIR-2 multispectral image (b) PRISM panchromatic image (c) Pansharpened image using GIHS method (d) Pansharpened image using SCFF method

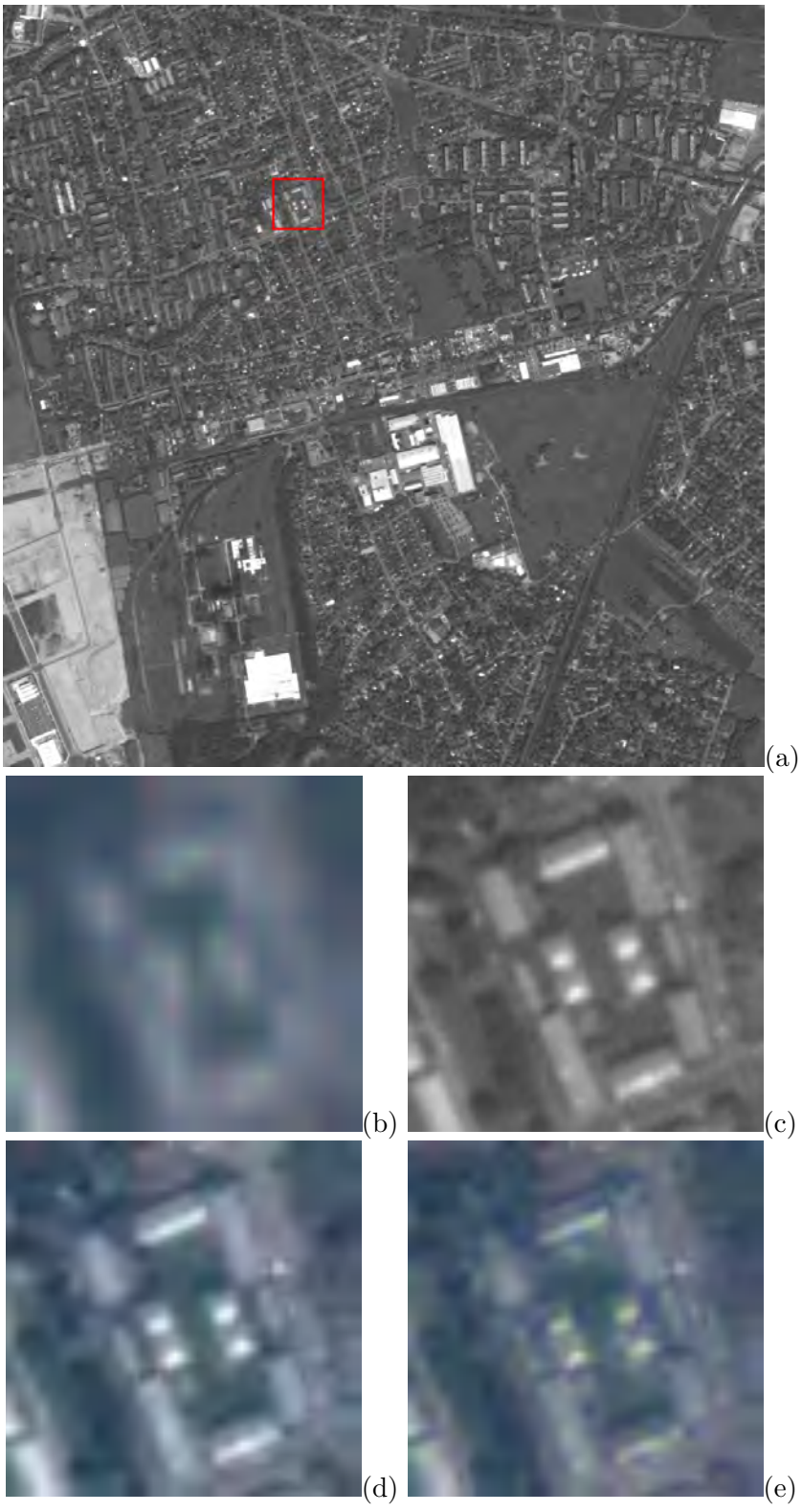

FIGURE 4.5: (a) Test area "Munich urban" showing location of detail image (b) Original AVNIR-2 multispectral image (c) original PRISM panchromatic image (d) Result images fused by GIHS methods (e) Result image fused by SCFF method

4.3 Computing performance

The image fusion algorithms are realized in the frame of this thesis in Matlab and calculated on an Intel i7-3770K machine featuring 16 Gigabyte RAM, SSD hard-drive and 64bit Windows 8 operating system. In order to measure the individual computing performance the calculations are applied to varying image sizes scaling by a factor of 2. The processing is performed in five iterations on every test area for every image size and the mean values for each image size are calculated. Figure 4.6 clearly displays the equal linear scaling of the two pansharpening methods depending on the overall pixel count of the test areas. The growth is described by a quadratic curve analog to the squaring pixel size of the images. The very high difference in the computing time results lies in the programmatical realization of the two algorithms. While the GIHS fusion can be performed by simple matrix addition and substraction, SCFF integrates a sliding window operation by the size of 3-by-3 pixels performed on each pixel of the image. It is obvious that the latter algorithm was not developed in regard to computing performance and leaves a large margin for codewise enhancements.

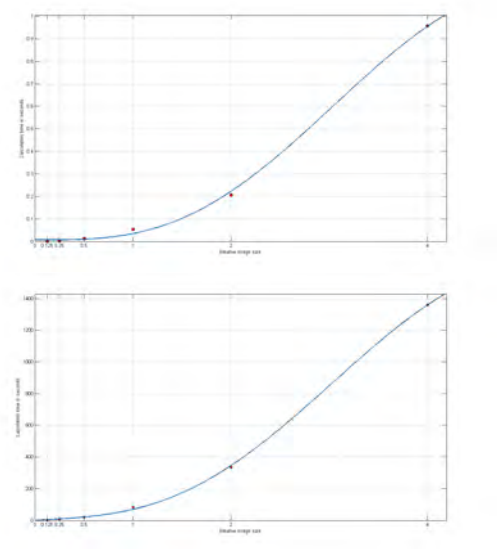

FIGURE 4.6: Computing performance of GIHS (top graph) and SCFF (bottom graph) pansharpening methods. The fitting curve shows the equal linear scaling related to relative image size, with 1 representing an edge length of the high-resolution image of 1024 pixels. Curve was calculated by the function $a \times (\sin(x - \pi) + b \times ((x - 10)^2)) + c \times (1)$. Coefficients for GIHS: $a = 0.2382, b = -0.012, c = 1.207$. Coefficients for SCFF: $a = 313.3, b = -17.52, c = 1752$. $RMSE(GIHS) = 0.01508, RMSE(SCFF) = 10.8$

Chapter 5

Discussion

5.1 The influence of co-registration errors on pansharpening methods

In the last chapter the performance of the two presented pansharpening methods was shown, revealing that SCFF constantly provides better results from a spectral point of view. As it also gives only slightly worse results as GIHS from a spatial point of view it allover can be seen as the more efficient algorithm.

In this chapter the analysis and discussion of how both fusion methods behave if the pansharpening process is conducted with source data that holds small and big co-registration errors. By manually measuring the geometric shift in both scenes the co-registration error was determined to average about 276 meters (regarding the unmatched level 1B product). The fact that corresponding multispectral and panchromatic images possessing an error to that extent can be seen as two completely different images manifests in Figures 5.1 and 5.2, showing that an evaluation of the pansharpening behavior cannot be conducted on the basis of this data.

This is further reinforced by the multispectral and panchromatic images both being shifted from the location of a reference image without (major) co-registration errors. Therefore a series of test areas containing increasing errors in the subpixel range of both sensors was synthetically generated by, starting from a quasi error-free image pair, shifting the multispectral image by the amount of 1 m in the x- and y-directions up to a displacement of 276 meters, matching the co-registration error of the original source data and providing a sufficient length of measurement to predict the pansharpening behaviour corning even greater co-registration errors. This was achieved by a stepwise manipulation of the coordinates of the correctly geocoded multispectral image and then resampling the multispectral image to its new location

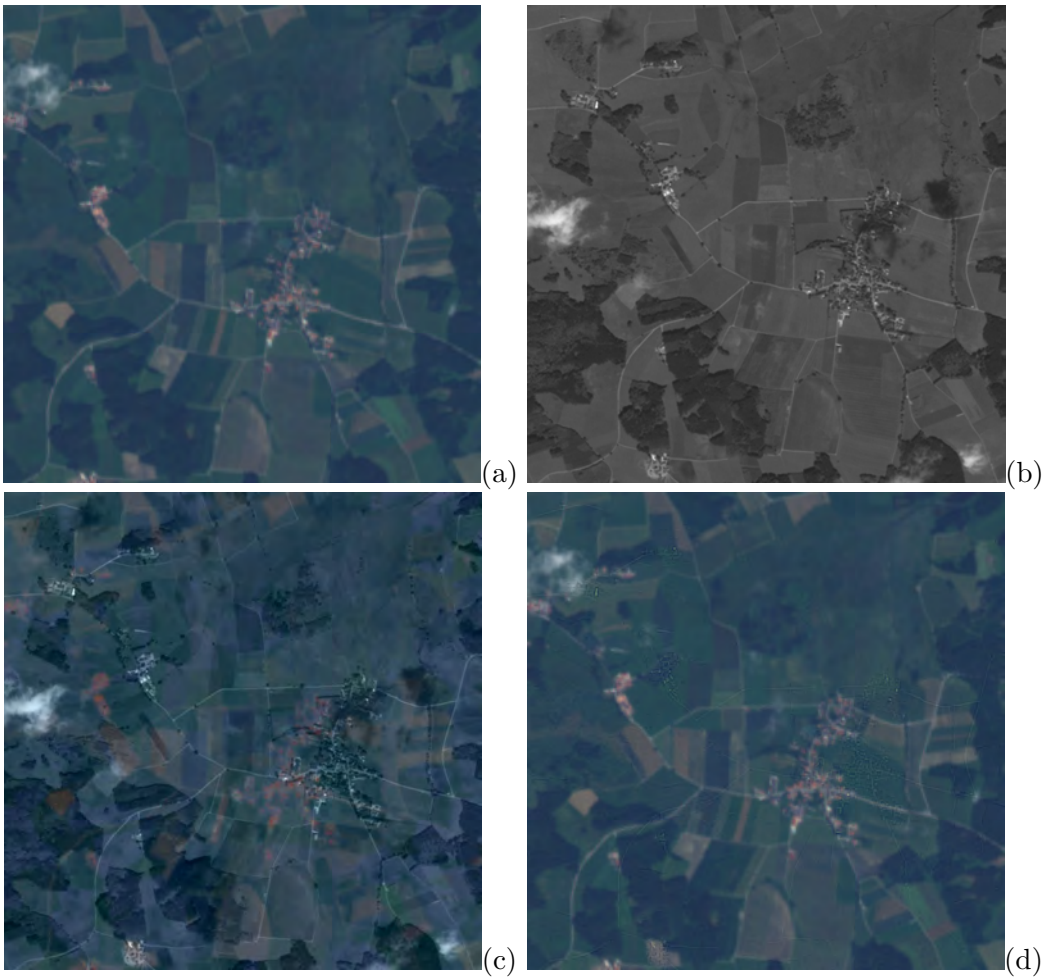

FIGURE 5.1: Test area "Munich agriculture" unmatched source data: (a) AVNIR-2 multispectral image (b) PRISM panchromatic image (c) Pansharpened image using GIHS method (d) Pansharpened image using SCFF method. The missing co-registration is clearly visible in the source images and the fused result images.

by nearest neighbour interpolation. The panchromatic image experiences no offset in this simulation. For every step the four presented quality measures were calculated, taking the correctly co-registered image pair as reference data.

Figures 5.3 and 5.4 show the performance of the GIHS and the SCFF pansharpening algorithms for the whole extent of the co-registration error. In both cases a clear tendency is visible. With a growing error the quality of the fused images falls following a continuous function. The difference arises in the response of the two fusion techniques to an increasing error.

While the GIHS method is generally producing result images with a lower quality (concerning the measures introduced in this thesis), it is not too sensible to changes in the size of a co-registration error. In both examples given the degradation

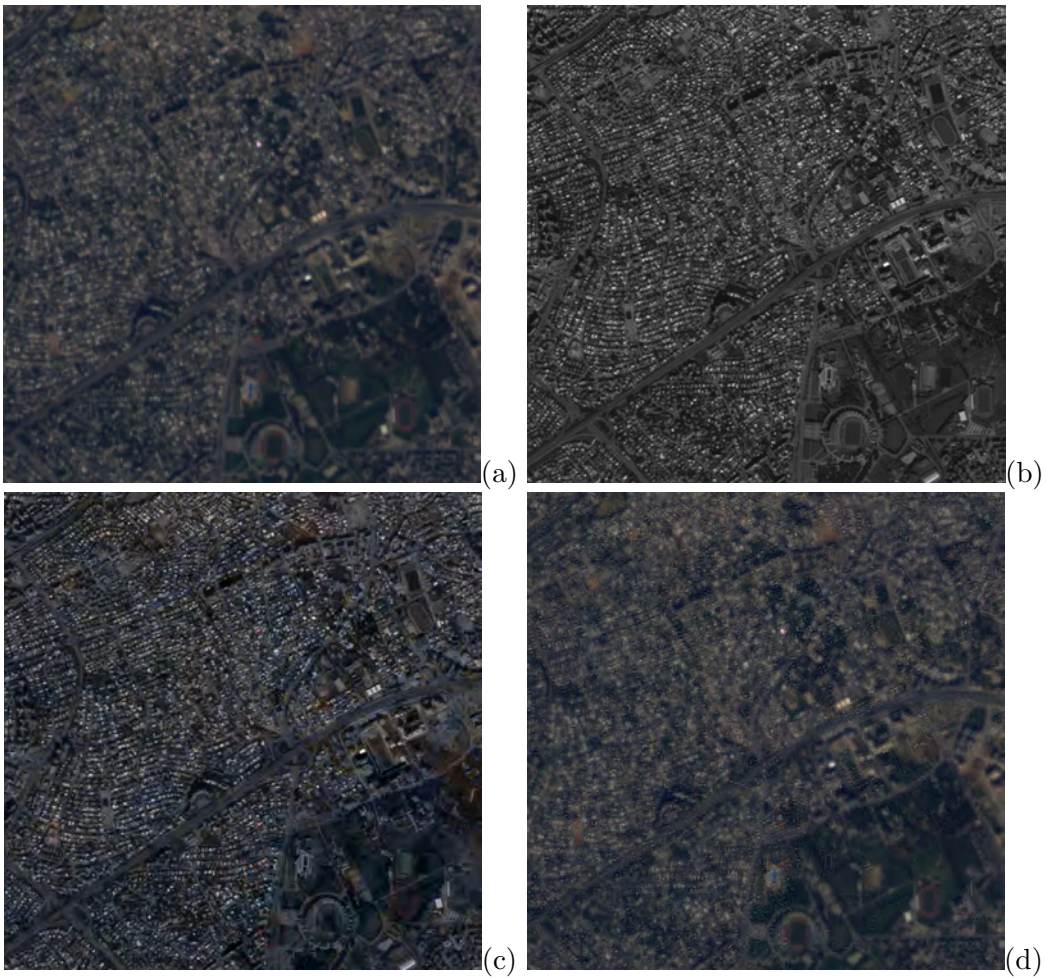

FIGURE 5.2: Test area "Tunis urban" unmatched source data: (a) AVNIR-2 multispectral image (b) PRISM panchromatic image (c) Pansharpened image using GIHS method (d) Pansharpened image using SCFF method. The missing co-registration is clearly visible in the source images and the fused result images.

especially for CC, ERGAS and Q-index is not very high considering even large error values. The by comparison rather fast aggravation of SAM can be explained by the overall lower performance of GIHS concerning spectral consistency. SCFF on the other hand suffers from a high vulnerability. All quality metrics are dropping in value very fast after just a few steps of error iteration. In the end they even adopt lower values than GIHS.

Although the shown graphs (Figues 5.3 and 5.4) depict a general behaviour of the two algorithms concerning co-registration errors, result images from source data with a co-registration error of this dimension, and thus in holding a shift of several pixels in the x- and y-direction, can by no means be regarded as satisfying. Further modern matching algorithms and processing chains are unlikely to produce errors

to that degree. Typical image matching methods achieve results in the range of 0.2 pixels regarding the lower resolution image [7, p. 64]. Therefore Figure 5.5 is giving a detailed view of the graphs in the range of zero to fifty meters of co-registration error, which conforms to five pixels of the AVNIR-2 multispectral source image.

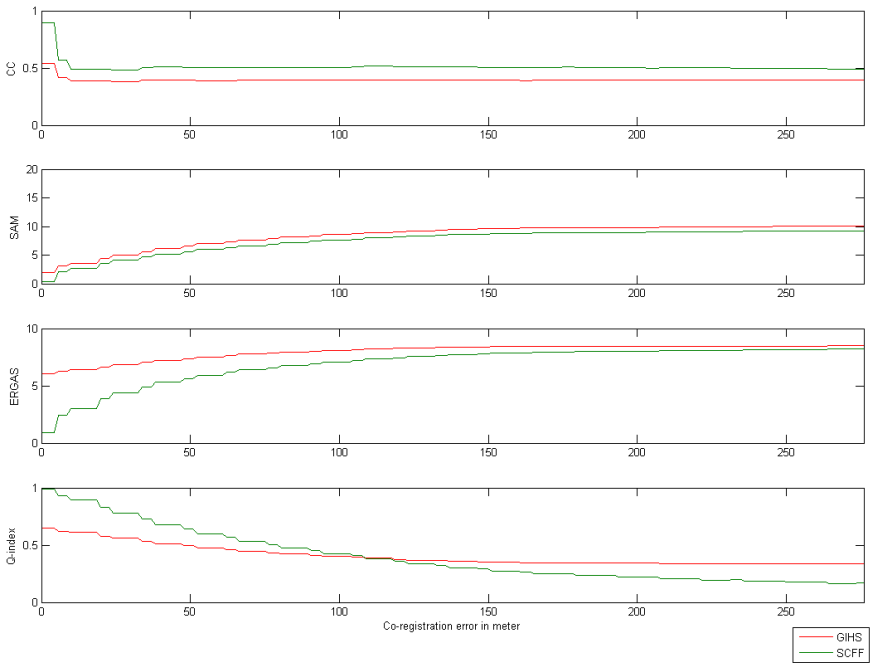

FIGURE 5.3: Test area "Munich agriculture": Performance of GIHS and SCFF pansharpening methods regarding a growing co-registration error (calculated in steps of 1.4 meters).

The stair-like appearance of the graphs is caused by two factors: One is that the underlying data is raster data, enabling a change detection only on a pixel-by-pixel basis. The second reason is that the shift is computed in steps of 1.4 meters of increasing co-registration error, which is actually in the sub-pixel space even of the high-resolution image, which features a ground pixel size of 2.5-by-2.5 square-meters. Therefore the shifted image has to be resampled to its new location which, as already mentioned, was done by nearest neighbour interpolation. The stair-like appearance can be seen as visualization of resampling effects. A major change in quality typically appears when a critical value of a co-registration error is passed.

These critical values are continually reached when the pixel border of the next adjacent low-resolution pixel is passed and after that when in that new pixel the two images are shifted further by one high-resolution pixel. As the mismatch in the

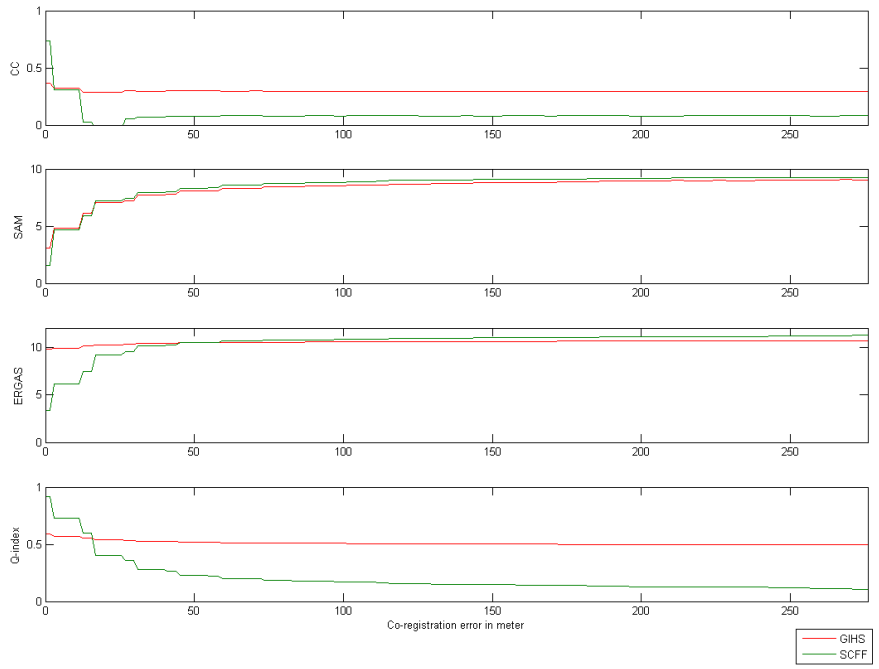

FIGURE 5.4: Test area "Tunis urban": Performance of GIHS and SCFF pansharpening methods regarding a growing co-registration error (calculated in steps of 1.4 meters).

ongoing example is an even shift in both the x- and the y-direction, the critical values lie at constant distances of 14.142 and 3.536 meters (illustrated in Figures 5.6 and 5.7). The quality change occurs when the co-registration error is equal or greater than the nearest critical value. It can be recognized in the example plots that the location of the very first quality shift differs in the both test areas. This is due to the fact that the test areas were cropped from the whole original scenes by means of world coordinates. Therefore it is not guaranteed that very first high-resolution pixel of the test area in the upper left corner of the sample region lies exactly in the upper left corner of a low-resolution pixel. This can evoke an initial shift between the multispectral and panchromatic sample area image, as the position of the of the panchromatic pixel may be located in the sub-pixel region of the low-resolution pixel. In this case the very first quality decrease occurs when the next relevant pixel border is passed.

As co-registration errors usually are not exactly even in the horizontal and vertical direction, the critical value of the first quality reduction of fused result

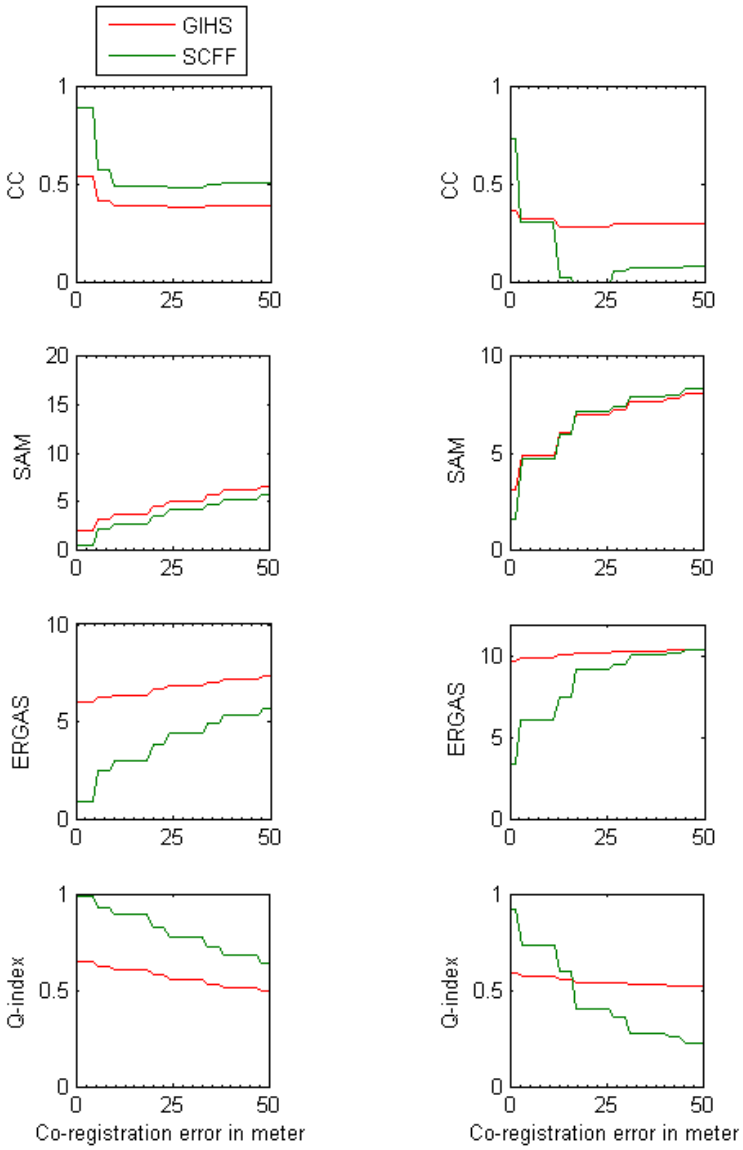

FIGURE 5.5: Quality graphs of the test areas "Munich agriculture" (left) and "Tunis urban" (right) showing the behaviour of the two image fusion algorithms over a range of 50 meters (calculated in steps of 1.4 meters).

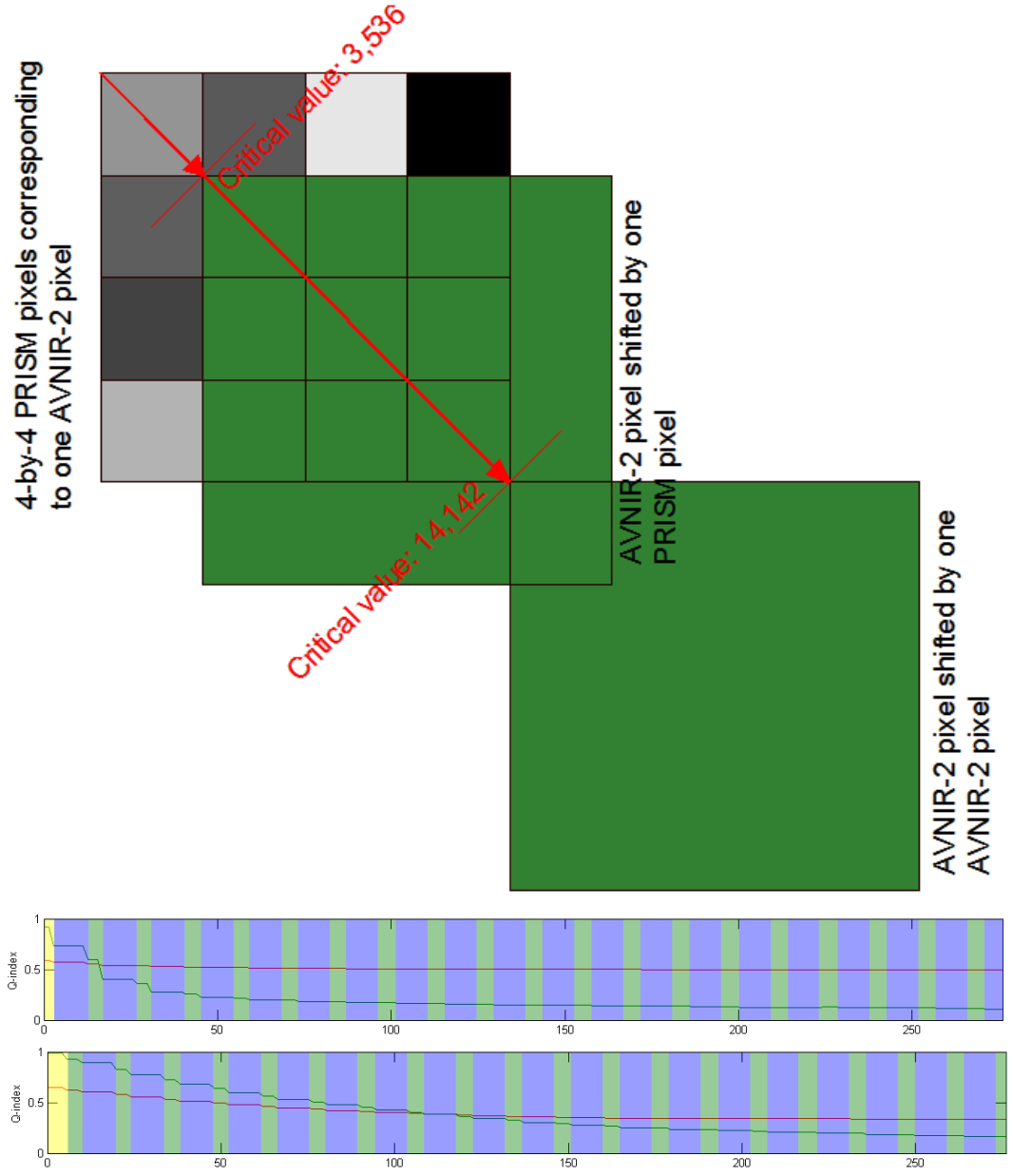

FIGURE 5.6: The upper schematics depict the pixel shift as conducted in this analysis. In the colored plots on the bottom (showing Q-index behaviours for both example test areas), the yellow section indicates the initial offset caused by coordinate cropping. The green and blue sections show the degrading of quality by equal step length, with green being the region of critical value one (3.536 meters) and blue being the distance of critical value two, counting from the last shift (10,606 meters = 14,142 meters - 3,536 meters). The green curve describes the SCFF, the red curve the GIHS behaviour.

images can be obtained as follows:

$$\begin{aligned} \alpha &= \arcsin\left(\frac{\sqrt{\Sigma_L^2}}{\sqrt{\Sigma_L^2+\Sigma_G^2}}\right) \\ C_G^{HR} &= \frac{P_{HR}}{\cos\alpha} \\ C_L^{HR} &= \frac{P_{HR}}{\sin\alpha} \\ C_G^{LR} &= \frac{P_{LR}}{\cos\alpha} \\ C_L^{LR} &= \frac{P_{LR}}{\sin\alpha} \end{aligned} \tag{5.1}$$

with

α = shift direction angle

Σ_L = lesser shift value

Σ_G = greater shift value

P_{HR} = ground pixel edge length of high-resolution source image

P_{LR} = ground pixel edge length of low-resolution source image

C_G^{HR} = high-resolution critical value in direction of the greater shift

C_L^{HR} = high-resolution critical value in direction of the lesser shift

C_G^{LE} = low-resolution critical value in direction of the greater shift

C_L^{LR} = low-resolution critical value in direction of the lesser shift.

As can be seen from the above equations the number of the continual quality change doubles when the co-registration errors in the x- and y- direction are not equal. Anyway the calculations in equation 5.1 only apply if the total error lies in the sub-pixel space of the source high-resolution image. Image pairs with individual co-registration errors in x- and/or y-direction exceeding the ground-pixel size of the panchromatic image can therefore be considered as inapplicable for pansharpening processes. Concerning the performance of the two introduced image fusion techniques, it can be stated that GIHS is the more stable method disregarding the general and heavy influence of co-registration errors on the results.

The overall performance of the methods not only depends on the degree of misregistration but also on the composition of the ground features. Areas with big homogeneous surfaces, like the field test area of in Munich scene in Figure 5.1, tend

to degrade in quality by a slower rate than ground structures featuring a high spatial frequency of image data.

5.2 Higher-level processing issues

With the characteristics of the two introduced satellite image fusion techniques concerning co-registration errors of the source data being analyzed, one step further is made by processing the result images to the next product level by applying AC (atmospheric correction). The atmospheric corrected test areas are then classified by means of index application of NDVI (Normalized Difference Vegetation Index) and EVI (Enhanced Vegetation Index). The intention is to reveal which influence the different degree of loss of spectral consistency concerning the two methods exerts on post processing applications.

5.2.1 Atmospheric correction

The atmospheric correction is calculated using the ENVI/IDL module ATCOR, based on the theoretical model for atmospheric correction of the same name, developed by Richter [9]. The whole process will only be summarized shortly as a detailed view on the topic of atmospheric correction would go beyond the scope of this work. In case of source image data originating from the PRISM and AVNIR-2 sensor following has to be considered. "The standard rural (continental) aerosol model is selected, because a reliable estimate of the aerosol type over land is not possible with a few VNIR (visible and near infrared) channels. The influence of the atmospheric water vapor column is very small for the AVNIR-2 channels, and since a water vapor map cannot be derived from an AVNIR-2 scene, a typical seasonal/-geographic value has to be taken. The same argument applies to the ozone column; again a fixed value pertaining to the selected climatology of the MODTRAN standard atmospheres is used" [9, p. 4080]. For both scenes the "Mid-Latitude Summer" atmosphere model was used, featuring a water vapor column of 2.92 cm at sea level. The general cycle of the atmospheric correction process can be layed out as:

1. Generation of masks for land, water, haze over land, cloud and satuared pixels
2. Calculation of aerosol optical thickness map at 550 nanometers
3. Optional haze removal
4. Application of surface reflectance retrieval

TABLE 5.1: Test areas "Munich" - reflectance standard deviation

	Method	Band 1	Band 2	Band 3	Band 4
Airport	MS	3.5	4.3	5.2	5.7
	GIHS	5.6	5.9	6.6	8.2
	SCFF	4.3	5.0	5.7	6.2
Cloud	MS	8.9	9.0	9.5	13.4
	GIHS	9.2	9.4	9.8	15.2
	SCFF	8.9	9.0	9.5	13.4
Agricult.	MS	1.3	1.8	2.6	9.1
	GIHS	2.3	2.7	3.4	9.4
	SCFF	1.4	1.9	2.7	9.1
Urban	MS	3.5	4.3	5.2	5.7
	GIHS	5.6	5.9	6.6	8.2
	SCFF	4.3	5.0	5.7	6.2
Water	MS	1.7	2.4	2.9	13.1
	GIHS	2.8	3.4	3.8	13.9
	SCFF	1.7	2.5	3.0	13.1
Forest	MS	1.5	2.1	2.6	7.5
	GIHS	2.6	3.0	3.4	8.3
	SCFF	1.6	2.2	2.7	7.5

TABLE 5.2: Test areas "Tunis" - reflectance standard deviation

	Method	Band 1	Band 2	Band 3	Band 4
Airport	MS	3.5	4.1	4.9	5.4
	GIHS	5.7	5.9	6.6	5.5
	SCFF	3.8	4.5	5.3	5.7
Mount.	MS	2.6	4.1	5.0	5.2
	GIHS	3.9	5.1	5.8	5.7
	SCFF	2.7	4.3	5.1	5.2
Desert	MS	1.6	2.5	3.3	2.6
	GIHS	2.5	3.3	4.0	2.7
	SCFF	1.6	2.5	3.3	2.6
Vege.	MS	1.0	1.7	2.2	3.1
	GIHS	1.7	2.1	2.7	3.0
	SCFF	1.0	1.7	2.3	3.1
Water	MS	2.3	3.7	5.1	6.7
	GIHS	2.8	4.1	5.4	6.8
	SCFF	2.3	3.8	5.1	6.7

As the individual calculations (e.g. water mask generation and water pixel detection) of the atmospheric correction process especially highly depend on the data contained in the blue and the near-infrared band of the processed image, ALOS scenes again are very suitable for the evaluation of pansharpening performance in relation to this type of higher-level processing. It was mentioned before that especially in these two channels the correlation between the multispectral and the pancharomatic sensor is very low. Therefore a pansharpening method with a better performance in the field of spectral consistency should be more capable to solve the under-determined statistical problem of high-resolution spectral reconstruction and thus deliver more consistent atmospheric correction results to the original multispectral image.

Tables 5.1 and 5.2 show the results of the AC application. Product level 2A images are depicted with the processed source multispectral image being upsampled to the size of the fused images by nearest-neighbour interpolation. The quality measure hereby is the standard deviation of reflection calculated for each individual band. The behaviour of GIHS and SCFF coincide with the insights got from the preceding analysis concerning the influence of co-registration error. The SCFF constantly delivers better results with some values even being equal to those of the original AVNIR-2 test area, like in the cloud sample of the Munich scene and the desert, vegetation and water samples of the Tunis scene. Atmospheric corrected images based on GIHS fusion on the other hand throughoutly posses standard deviations of reflection reaching values of 2.5 %. This difference between the two techniques again is caused by their diverse approach on solving the pansharpening problem. In both cases the highest difference values compared to the original multispectral image occur in band one and band four of the AVNIR-2 sensor which correspond to the blue and the near-infrared channel. This again shows that the nature of the underlying relative response functions of the involved optical satellite imaging sensors generally influence the outcome of pansharpening processes.

5.2.2 Index application

While the analysis of the atmospheric correction applied to fused images revealed that there are differences concerning the results of higher-level processing of variable pansharpened satellite images, the unequal performance as displayed in the course of this work can only be judged on a relative basis. Therefore the discussion in this part showw the absolute influence of errors concerning the spectral consistency of pansharpened images on classification based on atmospheric corrected source data.

5.2.2.1 NDVI and EVI

The NDVI (Normalized Difference Vegetation Index) is likely to be the most commonly used vegetation index in remote sensing applications. The NDVI is calculated pixel-wise by following formular:

$$NDVI = \frac{NIR - R}{NIR + R} \tag{5.2}$$

It shows the relative density of live vegetation on a ground patch of an optical satellite remote sensing scene. As a relative indicator it can obtain values in the interval of -1 to 1. As no still live vegetation causes NDVI values equal or nearing zero and lower these values are generally omitted when visualizing the index.

Viewing the images in Figure 5.7 depicting the results for the NDVI application there is almost no significant difference recognizable. Only the GIHS version of the test area from the Tunis scene appears to deliver slightly higher values for the classification. In order to visualize potential differences, absolute difference images between the original multispectral NDVI image and the GIHS respectively the SCFF NDVI image are calculated (Figure 5.9). These reveal that all presented pansharpening method results suffer from (small) errors concerning index application. Therefore it cannot be guaranteed that the fused images are suitable for higher-level processing of this kind.

EVI (Enhanced Vegetation Index) is, as can be supposed by its name, an improved vegetation index. It can be "considered as a modified NDVI but with improved sensitivity to high biomass regions and improved vegetation monitoring capability through a decoupling of the canopy background signal and a reduction in the atmospheric influences"[4, p. 1593f.]. The EVI value for every pixel in the source image is obtain by the equation:

$$EVI = 2 * \frac{NIR - R}{NIR + C_1 * R - C_2 * B + L} \tag{5.3}$$

with

$$\begin{aligned} L &= \text{canopy background adjustment term} \\ C_1, C_2 &= \text{coefficients of the aerosol resistance term} \end{aligned} \tag{5.4}$$

As the ENVI remote sensing software was used to generate the EVI images, the values for the coefficients L, C_1 and C_2 are respectively 1, 6 and 7.5. Looking at equation 5.3 it is obvious that the calculation follows the same strategy as NDVI and therefore relative ratios between the different multispectral bands are generated. Concerning the results of the index application the difference images in Figure 5.9

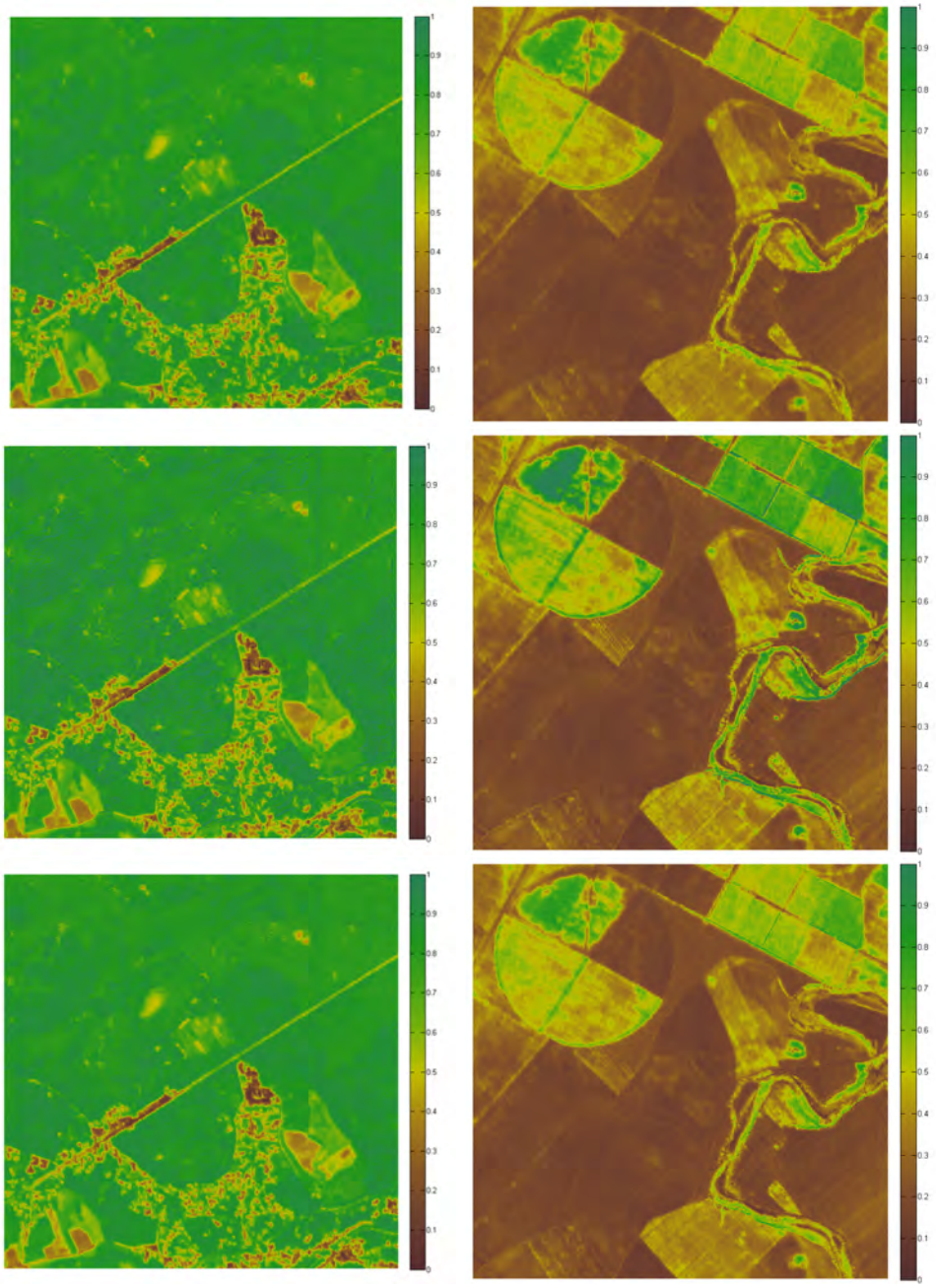

FIGURE 5.7: NDVI mapping for the sample ares "Munich forest" (left) and "Tunis vegetation" (right) displaying values from 0 to 1. From top to bottom the order of source multispectral image data is the original AVNIR-2 multispectral image, the pansharpened image using GIHS fusion and the fused image using the SCFF.

show that the Enhanced Vegetation Index, compared to NDVI, is much more stable concerning a certain spectral distortion of the source images.

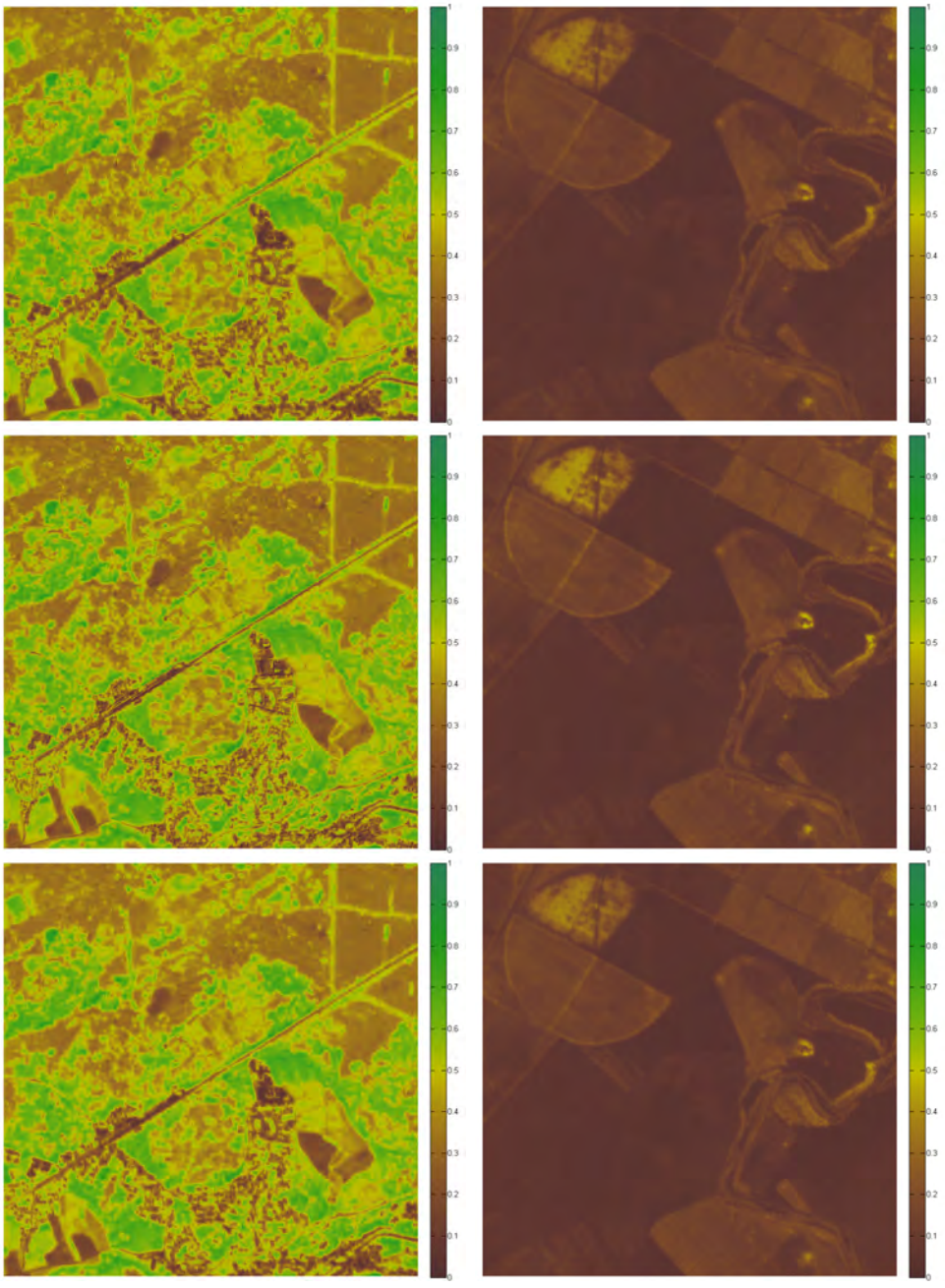

FIGURE 5.8: EVI mapping for the sample areas "Munich forest" (left) and "Tunis vegetation" (right) displaying values from 0 to 1. From top to bottom the order of source multispectral image data is the original AVNIR-2 multispectral image, the pansharpened image using GIHS fusion and the fused image using the SCFF.

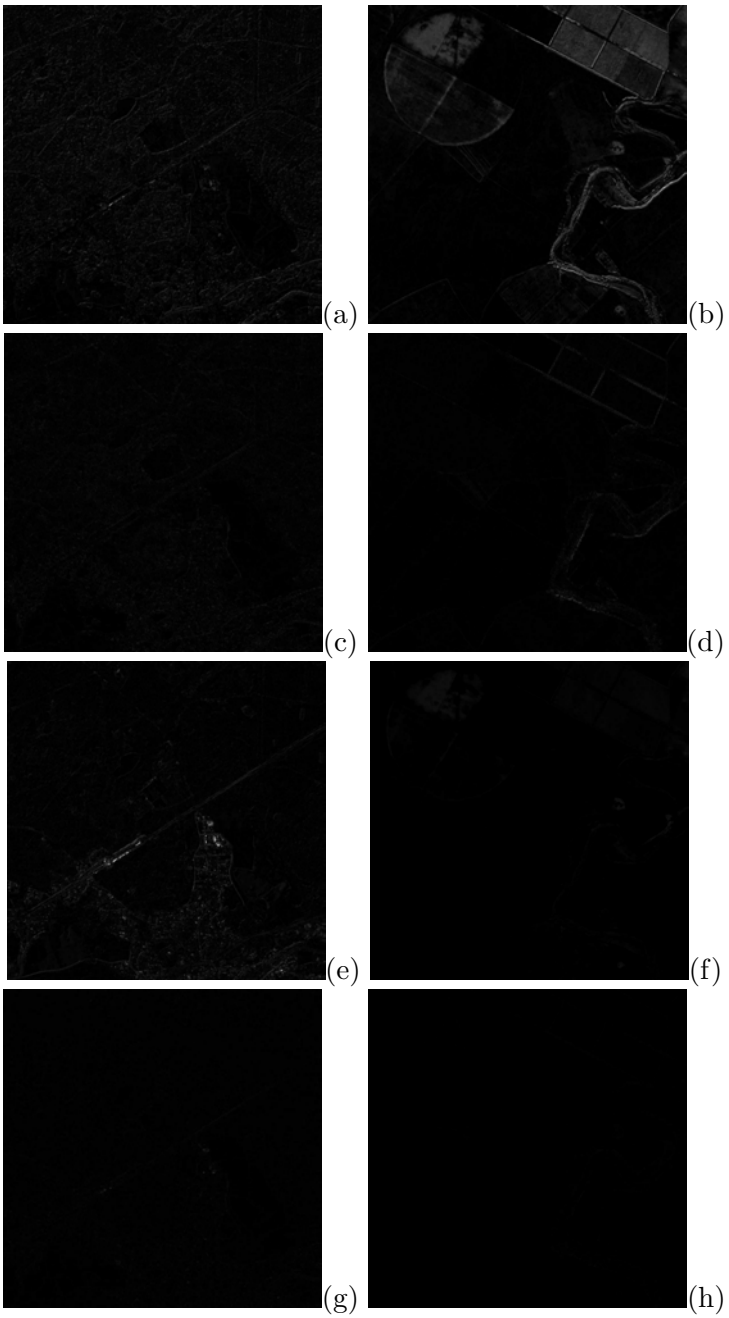

FIGURE 5.9: Difference of index images between the original low-resolution multispectral and the pansharpened images: (a) MS-GIHS NDVI "Munich forest" (b) MS-GIHS NDVI "Tunis vegetation (c) MS-SCFF NDVI "Munich forest" (d) MS-SCFF NDVI "Tunis vegetation" (e) MS-GIHS EVI "Munich forest" (f) MS-GIHS EVI "Tunis vegetation" (g) MS-SCFF EVI "Munich forest" (h) MS-SCFF EVI "Tunis vegetation"

Chapter 6

Conclusion

In the course of this work inherent challenges of optical Earth observation satellite image pansharpening were illustrated. They show that the quality of the results concerning spectral and spatial consistency depends very much on the composition of the source data and the used pansharpening principles of operation. Two distinctive methods, namely the Generalized Intensity-Hue-Saturation (GIHS) image fusion and a Spectrally Consistent Fusion Framework (SCFF) were analyzed regarding these aspects. It was discovered that SCFF consistently delivers more satisfying results compared to GIHS, only suffering from a slightly increased loss of geometric information. Typical quality indicators for the performance of image fusion were introduced to assess the processes. The overall better performance of SCFF comes with the drawback of a massively higher computation performance.

Further the influence of source data afflicted with co-registration errors was evaluated by simulating a stepwise mismatch between the high-resolution panchromatic and the lower resolution multispectral image in the sub-pixel range of the former. A general insight was gained that co-registration errors lying in the sub-pixel range of the high-resolution image do not influence the pansharpening result while errors of a greater margin decrease the quality very rapidly. This applies to the experiments conducted in this thesis. In terms of the presented methods, GIHS features a much higher stability concerning image mismatches.

Lastly the processing of the different pansharpening results to a higher product level, by first conducting atmospheric correction and then applying two different vegetation indices, showed that spectral distortion caused by the pansharpening process can but not necessarily will influence constitutive remote sensing applications.

While the tendencies of different pansharpening methods concerning a growing co-registration error was observed from a scientific point of view, the practical use of

optical satellite images mismatched to a greater extent can by denied. The results of the distinctive techniques regarding properly registered data on the other hand should not only be judged on quality metrics alone but also on the predetermined intended purpose of use of the images.

There surely is much space for future experiments to build on and expand the topic of this thesis. Constitutive analysis could observe the behaviour of other common image fusion techniques concerning co-registration errors. Possible examinations should also consider the development of robust pansharpening techniques and new pansharpening approaches like the fusion of panchromatic, multispectral and hyperspectral data or the combination of different optical satellite images with non-optical satellite data like SAR (Synthetic Aperture Radar).

Bibliography

[1] Aanæs, H., Sveinsson, J.R., Nielsen, A.A., Bovith, T., and Benediktsson, J.A., 2008: *Model-based satellite image fusion. Geoscience and Remote Sensing, IEEE Transactions on*, 46(5):pages 1336–1346. doi:10.1109/TGRS.2008.916475.

[2] Aanæs, Henrik. *http://www.imm.dtu.dk/∼aanes/*. Accessed: 24-03-2014.

[3] Amro, Israa, Mateos, Javier, Vega, Miguel, Molina, Rafael, and Katsaggelos, Aggelos K., 2011: *A survey of classical methods and new trends in pansharpening of multispectral images. EURASIP J. Adv. Sig. Proc.*, 2011:pages 79–100.

[4] Chikr El-Mezouar, M., Taleb, N., Kpalma, K., and Ronsin, J., 2011: *An IHS-based fusion for color distortion reduction and vegetation enhancement in IKONOS imagery. Geoscience and Remote Sensing, IEEE Transactions on*, 49(5):pages 1590–1602. doi:10.1109/TGRS.2010.2087029.

[5] Earth Observation Research Center (EORC), Japan Aerospace Exploration Agency (JAXA), 2-1-1, Sengen, Tsukuba-city, Ibaraki 305-8505 Japan, 2007: *ALOS User Handbook*.

[6] Licciardi, GiorgioAntonino, Khan, MuhammadMurtaza, Chanussot, Jocelyn, Montanvert, Annick, Condat, Laurent, and Jutten, Christian, 2012: *Fusion of hyperspectral and panchromatic images using multiresolution analysis and nonlinear pca band reduction. EURASIP Journal on Advances in Signal Processing*, 2012(1):pages 1–17. doi:10.1186/1687-6180-2012-207.

[7] Müller, Rupert, Krauß, Thomas, Schneider, Mathias, and Reinartz, Peter, 2012: *Automated georeferencing of optical satellite data with integrated sensor model improvement. Photogrammetric Engineering and Remote Sensing (PE&RS)*, 78(1):pages 61–74.

[8] Palubinskas, G. and Reinartz, P., 2011: *Multi-resolution, multi-sensor image fusion: general fusion framework*. In *Urban Remote Sensing Event (JURSE), 2011 Joint*. pages 313–316. doi:10.1109/JURSE.2011.5764782.

[9] Schwind, P., Schneider, M., Palubinskas, G., Storch, T., Müller, R., and Richter, R., 2009: *Processors for alos optical data: Deconvolution, DEM generation, orthorectification, and atmospheric correction. Geoscience and Remote Sensing, IEEE Transactions on*, 47(12):pages 4074–4082. doi:10.1109/TGRS.2009.2015941.

[10] Tu, Te-Ming, Huang, P.S., Hung, Chung-Ling, and Chang, Chien-Ping, 2004: *A fast intensity-hue-saturation fusion technique with spectral adjustment for IKONOS imagery. Geoscience and Remote Sensing Letters, IEEE*, 1(4):pages 309–312. doi:10.1109/LGRS.2004.834804.

[11] Tu, Te-Ming, Su, Shun-Chi, Shyu, Hsuen-Chyun, and Huang, Ping S., 2001: *A new look at IHS-like image fusion methods. Information Fusion*, 2(3):pages 177–186. doi:http://dx.doi.org/10.1016/S1566-2535(01)00036-7.

[12] Wald, L., 1997: *Fusion of satellite images of different spatial resolutions: assessing the quality of resulting images*. volume 63. pages 691–699.

[13] Wald, L., 2000: *Quality of high resolution synthesised images: Is there a simple criterion ?* In *proceedings of the third conference "Fusion of Earth data: merging point measurements, raster maps and remotely sensed images", Sophia Antipolis, France*. pages 99–103.

[14] Wang, Zhou and Bovik, A.C., 2002: *A universal image quality index. Signal Processing Letters, IEEE*, 9(3):pages 81–84. doi:10.1109/97.995823.

[15] Yuhas R.H., Boardman J.W., Goetz A.F.H., 1992: *Discrimination among semi-arid landscape endmembers using the spectral angle mapper (sam) algorithm*:pages 147–149.

[16] Zhu, X.X. and Bamler, R., 2013: *A sparse image fusion algorithm with application to pan-sharpening. Geoscience and Remote Sensing, IEEE Transactions on*, 51(5):pages 2827–2836. doi:10.1109/TGRS.2012.2213604.

Fakultät für Geoinformation

HOCHSCHULE FÜR ANGEWANDTE WISSENSCHAFTEN MÜNCHEN

Erklärung

gemäß § 15 Abs. 5 APO in Zusammenhang mit § 35 Abs. 7 RaPO

Name: .....

Vorname: .....

Geburtsdatum: .....

Studiengang: .....

Studiengruppe: .....

Matrikel-Nr.: .....

Winter-/Sommersemester: .....

Betreuer/in: .....

Hiermit erkläre ich, dass ich die Bachelorarbeit selbständig verfasst, noch nicht anderweitig für Prüfungszwecke vorgelegt, keine anderen als die angegebenen Quellen oder Hilfsmittel benutzt, sowie wörtliche und sinngemäße Zitate als solche gekennzeichnet habe.

....

Ort, Datum **Unterschrift**

Bitte unterschreiben Sie diese Erklärung und geben Sie diese zusammen mit der Bachelorarbeit beim Betreuer / bei der Betreuerin ab